

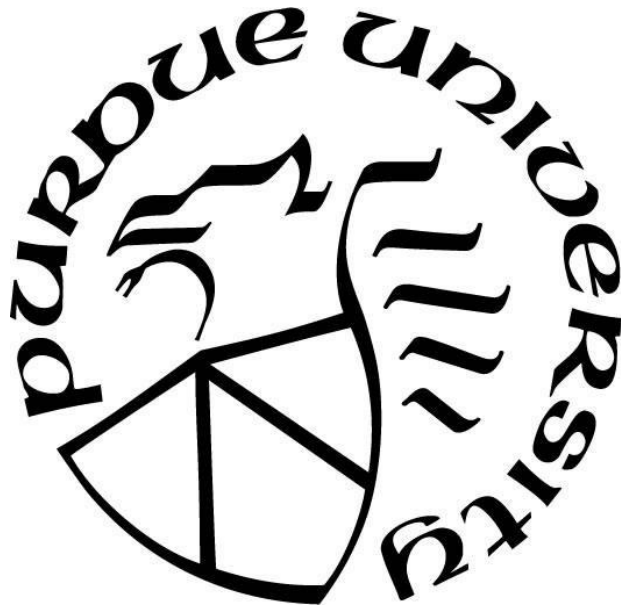
**INTERIOR ENVIRONMENT MODELING FOR RESILIENT EXTRA-  
TERRESTRIAL HABITATS**

by  
**Amanda Lial**

**A Thesis**

*Submitted to the Faculty of Purdue University  
In Partial Fulfillment of the Requirements for the degree of*

**Master of Science in Mechanical Engineering**



School of Mechanical Engineering  
West Lafayette, Indiana  
December 2022

**THE PURDUE UNIVERSITY GRADUATE SCHOOL  
STATEMENT OF COMMITTEE APPROVAL**

**Dr. Shirley Dyke, Co-Chair**

School of Mechanical Engineering

**Dr. Davide Ziviani, Co-Chair**

School of Mechanical Engineering

**Dr. Mohammad Reza Jahanshahi**

Lyles School of Civil Engineering

**Approved by:**

Dr. Nicole L. Key

*Dedicated to my mother, grandmother, Nikki, Laura, Luca, Jaewon, and everyone who has supported me. A special thank you to the United States Air Force Academy for providing me with this great opportunity.*

*“When I look at your heavens, the work of your fingers,  
the moon and the stars, which you have set in place,  
what is man that you are mindful of him,  
and the son of man that you care for him?”*

*Psalm 8:3-4*

*Here’s a toast to those we boast.*

## **ACKNOWLEDGMENTS**

This work is funded by NASA under grant or cooperative agreement award number 80NSSC19K1076.

# TABLE OF CONTENTS

LIST OF TABLES .....	7
LIST OF FIGURES .....	8
ABSTRACT .....	13
1. INTRODUCTION .....	14
1.1 Motivation .....	14
1.2 Resilient ExtraTerrestrial Habitat Institute .....	15
1.3 Modular Coupled Virtual Testbed Description .....	16
1.4 Cyber-Physical Testbed Description .....	19
1.5 Thesis Objectives and Approach .....	19
2. LITERATURE REVIEW .....	21
2.1 Thermal Modeling Inspiration .....	21
2.2 Pressure Modeling Inspiration .....	21
3. METHODOLOGY .....	23
3.1. Model Description .....	23
3.1.1 Habitat Interior Environment Model Disturbances .....	25
3.2 Temperature Model .....	29
3.2.1 Interior Environment Thermal Model .....	29
3.2.2 Airlock Thermal Model .....	37
3.2.3 Natural Convection Between Interior Environment and Airlock .....	38
3.3 Pressure Model .....	39
3.2.1 Interior Environment Pressure Model .....	39
3.2.2 Meteorite Air Leakage Pressure Model .....	40
3.3 Coupling Pressure and Temperature .....	43
4. HIEM MODEL VALIDATION USING CPT MODEL .....	46
4.1 Experimental Setup .....	46
4.2 Thermal Model Updates for the Pressure Box .....	49
4.3 Methodology: Constant Mass Flow Rate .....	50
4.3.1 Pressure Box Data Collected .....	51

4.3.2 Pressure Box Model Results .....	56
5. MCVT RESULTS .....	62
6. CONCLUSION AND FUTURE WORK.....	74
APPENDIX A: TEST PROCEDURES .....	76
APPENDIX B: PRESSURE BOX DRAWING WITH DIMENSIONS.....	79
APPENDIX C: PRESSURE BOX RC VALUES .....	81
REFERENCES.....	82

## LIST OF TABLES

Table 1-The EMS subsystem models and their descriptions for MCVT [11] .....	18
Table 2-The HMS subsystem models and agent descriptions for MCVT [11] .....	18
Table 3-Fire Disturbance Information [11].....	26
Table 4-Meteorite Impact Disturbance Information [10] .....	26
Table 5-Airlock Failure Disturbance Information .....	29
Table 6-Thermal resistance and unit thermal capacitance values.....	35
Table 7-Radiative and convective fraction values .....	36
Table 8-Internal gains values .....	36
Table 9-Fire calculation values .....	37
Table 10-Dynamic pressure values.....	42
Table 11-List of sensors and hardware used [33] .....	47
Table 12-List of experiments conducted.....	48

## LIST OF FIGURES

Figure 1-Walt Disney’s Mars and Beyond comic cover [7] .....	14
Figure 2-Whole MCVT Simulink model with the subsystems.....	17
Figure 3-CPT flowchart for RETHi habitat resilience design [12].....	19
Figure 4-Depiction of HIEM inputs and outputs with neighboring subsystems .....	24
Figure 5-Simulink interior environment model .....	24
Figure 6-Simplified schematic showing the separation of the interior environment and airlock ..	27
Figure 7-Drawing of the lunar habitat showing the inner and outer doors .....	28
Figure 8-Conceptual 3D view of a lunar habitat with the addition of an airlock .....	28
Figure 9-Interaction of gains and loads in the interior environment [24].....	29
Figure 10-Sensible cooling calculation components [24].....	31
Figure 11- Zone air heat balance visualization [24] .....	31
Figure 12-Heat flows for the thermal network [24].....	32
Figure 13- Thermal network of a single zone cooling load.....	32
Figure 14-Thermal network for the interior environment.....	33
Figure 15- Structural subsystem nodal locations .....	34
Figure 16-Airlock thermal network .....	37
Figure 17-Air slug in lunar habitat opening.....	41
Figure 18-Pressure box .....	46
Figure 19-Sample signal sent to mass flow controller.....	47
Figure 20-Unfiltered data (left) and filtered data (right) .....	48
Figure 21-Thermal network for the pressure box .....	49

Figure 22-Temperature (left) and pressure (right) for the pressure box at 0 Volts.....	51
Figure 23-Mass flow rate (left) and effective area (right) of pressure box for 0 Volts .....	52
Figure 24-Temperature (a), pressure (b), mass flow rate (c), and effective area (d) of the pressure box at 1 Volt.....	53
Figure 25-Temperature (a), pressure (b), mass flow rate (c), and effective area (d) of the pressure box at 2 Volts .....	54
Figure 26-Temperature (a), pressure (b), mass flow rate (c), and effective area (d) of the pressure box at 3 Volts .....	55
Figure 27-Temperature (a) and pressure (b) for 0-Volt pressure box model.....	56
Figure 28-Data comparison of temperature (a) and pressure (b) for 0-Volts .....	57
Figure 29-Temperature (a) and pressure (b) for 1-Volt pressure box model.....	57
Figure 30-Data of temperature (a) and pressure (b) comparison for 1-Volt.....	58
Figure 31-Temperature (a) and pressure (b) for 2-Volt pressure box model.....	58
Figure 32-Data comparison of temperature (a) and pressure (b) for 2-Volts .....	59
Figure 33-Temperature (a) and pressure (b) for 3-Volt pressure box model.....	60
Figure 34-Data comparison of temperature (a) and pressure (b) for 3-Volts .....	60
Figure 35-Temperature of HIEM (a) and the airlock (b) under normal conditions.....	62
Figure 36. Pressure of HIEM (a) and the airlock (b) under normal conditions .....	63
Figure 37-ECLSS thermal load distributed to HIEM and the airlock under normal conditions ...	63
Figure 38-Fire radius for fire intensity level 2.....	64
Figure 39. Temperature of HIEM (a) and the airlock (b) for fire intensity level 2 .....	64
Figure 40. Pressure of the HIEM (a) and the airlock (b) for fire intensity level 2 .....	65
Figure 41. Fire radius for fire intensity level 3 .....	65

Figure 42- Temperature of HIEM (a) and the airlock (b) for fire intensity level 3 .....	66
Figure 43- Pressure of the HIEM (a) and the airlock (b) for fire intensity level 3 .....	66
Figure 44. Fire radius for fire intensity level 4 .....	67
Figure 45. Temperature of HIEM (a) and the airlock (b) for fire intensity level 4 .....	67
Figure 46. Pressure of HIEM (a) and the airlock (b) for fire intensity level 4 .....	68
Figure 47. Fire radius for fire intensity level 5 .....	68
Figure 48- Temperature of HIEM (a) and the airlock (b) for fire intensity level 5 .....	69
Figure 49. Pressure of HIEM (a) and the airlock (b) for fire intensity level 5 .....	69
Figure 50. Temperature of HIEM (a) and the airlock (b) for meteorite intensity level 4 .....	70
Figure 51. Pressure of HIEM (a) and the airlock (b) for meteorite intensity level 4 .....	70
Figure 52. Temperature of HIEM (a) and the airlock (b) for meteorite intensity level 5 .....	71
Figure 53. Pressure of HIEM (a) and the airlock (b) for meteorite intensity level 5 .....	71
Figure 54. Temperature of HIEM (a) and the airlock (b) for airlock failure intensity level .....	72
Figure 55. Pressure of HIEM (a) and the airlock (b) for airlock failure intensity level 2 .....	72
Figure 56. ECLSS thermal load for airlock failure intensity level 3 .....	73
Figure 57- Temperature of HIEM (a) and the airlock (b) for airlock failure intensity level .....	73
Figure 58- Pressure of HIEM (a) and the airlock (b) for airlock failure intensity level 3 .....	73

## NOMENCLATURE

### Symbols:

$A$	Area [m <sup>2</sup> ]
$C$	Thermal capacitance [Btu / °F]
$cd$	Discharge coefficient [-]
$C_L$	Loss coefficient [-]
$Gr$	Grashof[-]
$L$	Length [m]
$\dot{m}$	Mass flow rate [kg/s]
$\mu$	Viscosity [Pa-s]
$Nu$	Nusselt number [-]
$P$	Pressure [Pa]
$Pr$	Prandtl number [-]
$Q$	Volumetric flow rate [m <sup>3</sup> /s]
$R$	Thermal Resistance [hr-°F/Btu]
$Ra$	Rayleigh's number [-]
$\rho$	Density [kg/m <sup>3</sup> ]
$T$	Temperature [°C]

### Abbreviations:

CPT	Cyber-physical testbed
ECLSS	Environmental control life support system
EMS	Electro-mechanical systems
HIEM	Habitat interior environment model
HMS	Health management systems
ISS	International space station
MCVT	Modular coupled virtual testbed
NASA	National aeronautics and space administration
NRH	Notional real habitat

RETHi  
UK

Resilient extra-terrestrial habitat institute  
United Kingdom

## ABSTRACT

There are several challenges that occur when creating extraterrestrial structures that are not relevant to terrestrial applications. The Resilient Extra-Terrestrial Habitat Institute is a NASA funded research project focused on developing resilient lunar habitats. In order to develop these deep-space structures, many considerations have to be made to account for scenarios that are not relevant to Earth. Such scenarios include meteorite impacts, moonquakes, radiation, and moon dust accumulation. To observe possible consequences of these disruptions, RETHi established a modular coupled virtual testbed to monitor the effects of different deep-space related situations. MCVT is a computer model of a lunar habitat that uses a system-of-systems approach to examine the impacts of these scenarios. Currently, MCVT is developing methods to confront these extraterrestrial situations by utilizing robotic agents and expanding upon a variety of safety responses to increase resiliency. RETHi also utilizes a cyber physical testbed to run cyber-physical experiments to validate the approaches used in MCVT.

One of the numerous models in MCVT is the Habitat Interior Environment Model. HIEM monitors the interior environment of the lunar structure using physics-based calculations and inputs from its surroundings. There are three main disturbances that directly affect the interior environment—fire within the dome, meteorite impacts, and airlock failure. Such scenarios either increase or decrease the temperature and pressure. This data is then forwarded to other subsystems for further evaluation. HIEM can be remodeled to fit the pressure box in the cyber physical testbed. By doing so, it is then possible to validate the pressure leakage calculations used in HIEM using experimental data. HIEM is specifically designed to the lunar habitat currently in development; however, the model can be refitted to a variety of applications such as terrestrial, aerospace, space, and marine.

# 1. INTRODUCTION

## 1.1 Motivation

Since the beginning, mankind has had a fascination with the heavens—even before Galileo Galilei used his telescope to observe the craters of earth’s moon and the moons of Jupiter [1, 2]. Such astronomical passion led to riots in the church when Nicolaus Copernicus discovered that the geocentric universe was in fact heliocentric [3]. Man was so inspired by the heavenly bodies in the sky that they personified and named them after Greek and Roman gods and goddesses [4]. As technology advanced, man grew closer to the heavens. Coupling man’s fascination with space and his competitive nature ultimately led to the dawn of the space age with the launch of the Soviet Union’s Sputnik 1 in 1957 [5]. The space race continued until 21 July 1969 when the United States put the first man on the moon [6]. Yet, before man landed on the moon, humans have dreamed of settling in the vastness of space. Figure 1 shows Walt Disney’s *Mars and Beyond* comic from 1957 which depicts man exploring Mars and other planets in search of answers from the great beyond [7].

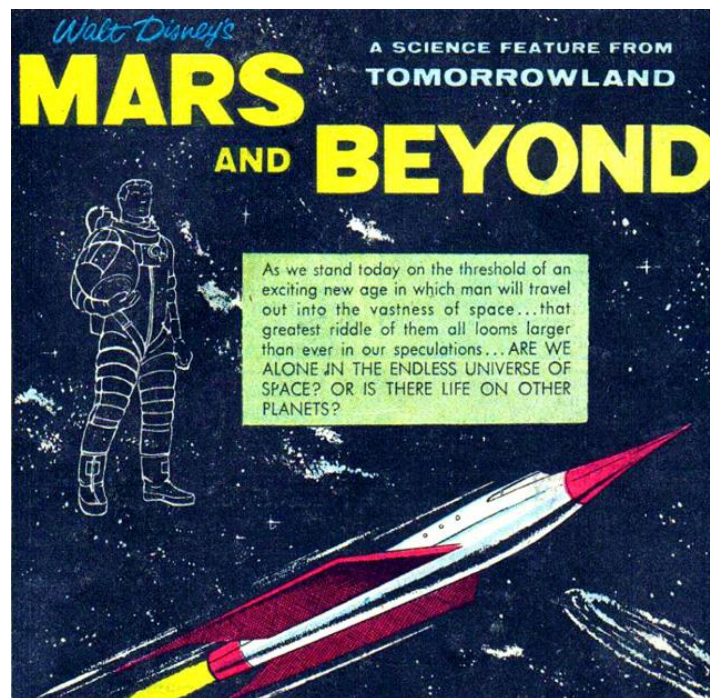


Figure 1-Walt Disney’s Mars and Beyond comic cover [7]

Since the dawn of the space age, humans have craved extraterrestrial habitation and exploration. The creation of the ISS is evidence enough of man's handful of attempts to reside outside of the relatively safe confines of Earth. Astronauts are known to push themselves physically and mentally to board and stay on the ISS—setting duration records in the process [8]. However, humans are far away from settling on the moon, let alone Mars. Nevertheless, numerous space programs have funded research for such endeavors. NASA has funded the Resilient ExtraTerrestrial Habitat Institute for Purdue University, University of Connecticut, Harvard University, and The University of Texas at San Antonio to conduct research toward realizing deep-space habitation by humankind.

## **1.2 Resilient ExtraTerrestrial Habitat Institute**

The Resilient ExtraTerrestrial Habitat Institute was established in 2019 to further mankind's ability to safely inhabit sites away our earthly home—using the moon as a steppingstone [9]. The mission of RETHi is “to develop the technologies needed to establish Resilient ExtraTerrestrial Habitats” [10]. RETHi aims to design SmartHabs, a class of space habitats that can autonomously recognize and respond to various disruptions that may or may not occur on Earth (earthquakes/moonquakes, meteorite impacts, etc) [9]. In order to create SmartHabs, RETHi is focused on obtaining the knowhow to develop such technologies as well as investigating the system features such as SmartHab architecture [9]. Fortunately, mankind has had thousands of years of engineering experiences that have contributed to our understanding of the special needs for terrestrial habitation that allow them to withstand a variety of terrestrial hazards such as earthquakes, high winds, and storms [9]. These experiences must be leveraged in the development of SmartHabs. However, lunar habitation involves numerous complications man has yet to encounter on Earth [9]. Unlike terrestrial habitats, structures in space are under constant war-like threats due to the extremes of the environment away from Earth's atmospheric protection [9]. Furthermore, inhabiting areas beyond Earth's protective and reliable environment cause delays and uncertainties in access to food, water, and oxygen [9]. Consequently, RETHi must augment the capabilities of the SmartHabs for resilience and sustainability by implementing algorithms. By doing so, researchers can determine essential information from different disturbances used for the repair and maintenance robots [9]. Numerous disruptions (e.g., fire) are simulated within the interior environment, as well as moonquakes, micro-meteorite impacts, dust accumulation, and radiation to evaluate the effects of these disruption scenarios and to choose the most appropriate among

several repair methods [9].

### 1.3 Modular Coupled Virtual Testbed Description

In order to verify pre-existing ideas and study the complex interactions that influence how a lunar habitat can gain the ability to recognize and respond to various disturbance scenarios, RETHi has developed a numerical model of a notional real habitat system. NRH is a conceptual way of theorizing the lunar habitats. MCVT is a scaled computational model of NRH to represent the lunar habitat with different disturbances [11]. MCVT represents a system-of-systems and is comprised of various physics-based models that interact with one another using signals representing physical interactions and by propagating necessary disturbance information. MCVT helps to fill the knowledge gaps between terrestrial living and lunar living. This can be used to educate man about extraterrestrial habitation without having to spend excess time and money on physical trial and error constructions. MCVT (version 6.2) has the ability to perform complex simulations based on 6 disruptions and 16 disruption scenarios. These scenarios are being used by researchers to develop a resilience framework for SmartHab design and verification, including architecture, decision-making, and robotics [11].

There are three branches within MCVT: electro-mechanical systems, health management systems, and agent systems. EMS systems are included to propagate the physical response through the habitat system including responses from the protective regolith system, structural system, habitat interior environment system, environmental control and life support system, and power system in Simulink as shown in Figure 2 [11]. The disturbance model is an input to the subsystems to initiate the disturbances that disperse throughout the habitat through the other interacting subsystems in EMS. Various disturbances and their consequences are modeled—including meteorite impact, sensor failure, dust accumulation, fire, moonquake, and airlock leakage. [11]. On page 18, Table 1 describes each of the EMS subsystems. In the MCVT, HMS involves communications, command and control, and data storage. It aids researchers in the decision-making process and is vital supporting autonomy in the habitat system [11]. The agents modeled in MCVT have the ability to alter the physical habitat (such as decreasing the meteorite

impact hole radius) and are either human or robotic in the simulations. Table 2 describes each of

the HMS components and the agents.

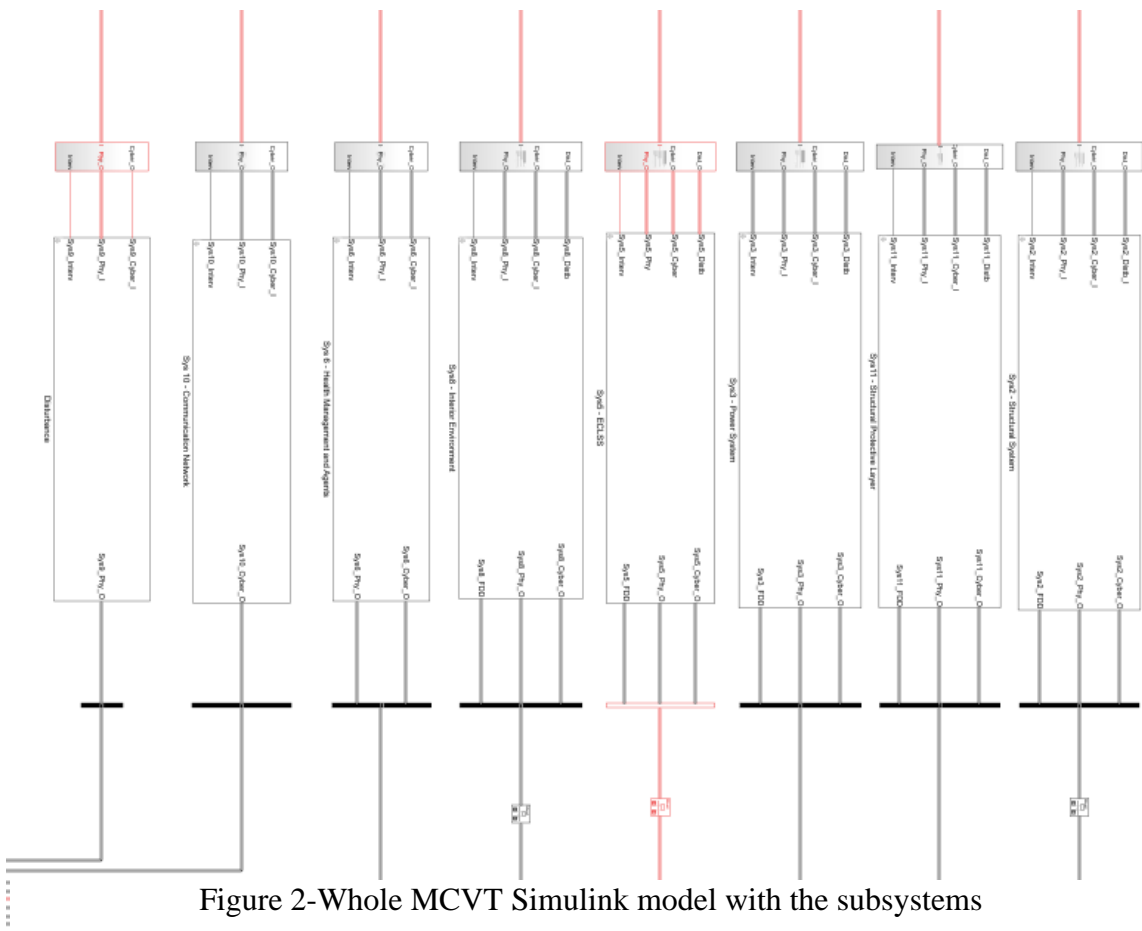


Figure 2-Whole MCVT Simulink model with the subsystems

Table 1-The EMS subsystem models and their descriptions for MCVT [11]

<b>Subsystem</b>	<b>Model Description</b>
Structural Protective Layer	Models the protective regolith layer behavior
Structural System	Tracks the habitat structure's mechanical and thermal properties
Power System	Models the generation of solar and nuclear power generation and monitors power distribution
Interior Environment	Models the temperature and pressure within the habitat
ECLSS	Ensures the temperature and pressure are within a comfortable range through pressure and temperature management
Disturbance Model	Initiates the disturbances at various intensities and directs the propagation throughout the subsystems

Table 2-The HMS subsystem models and agent descriptions for MCVT [11]

<b>Subsystem</b>	<b>Description</b>
Command and Control	Determines actions for maintain or restoring system functionality
Communication Network	Emulates the communication infrastructure used to enable data flow
Data Repository	Stores sensor data and fault detection and diagnosis information
Agent	Characterize the actions of the human and robotic agents

## 1.4 Cyber-Physical Testbed Description

RETHi has also invested in the design and development of a novel cyber-physical testbed which couples cyber modeling and physical testing to conduct target experiments [12]. By incorporating cyber models, it is not necessary to spend excess money strictly on physical testing. This testbed assists researchers to validate the methods used for the MCVT subsystems and their interactions while in the laboratory rather than the lunar surface—thereby saving time and money. Cyber-physical testing allows researchers to use the current knowledge of the physical world to better understand concepts of physical systems that they have limited knowledge of [12]. By coupling the physical world with the cyber, it is then possible to improve our understanding of the complicated dynamic interactions. CPT technology is important for studying SmartHabs and for validating new concepts of deep space habitats since we currently lack the technology and knowledge for such applications. Realistic experiments to gain crucial deep space habitation disturbance experiences would be either impossible or especially costly. Cyber-physical testing reduces the need for physical trial and error so that researchers can evaluate different design approaches in simulated hazardous and extreme environments in a timely, cost-effective manner. RETHi will use the CPT to validate the resilient design framework, evaluate health management algorithms, and design a resilient habitat system [12]. Figure 3 shows the process of how CPT will be used within RETHi.

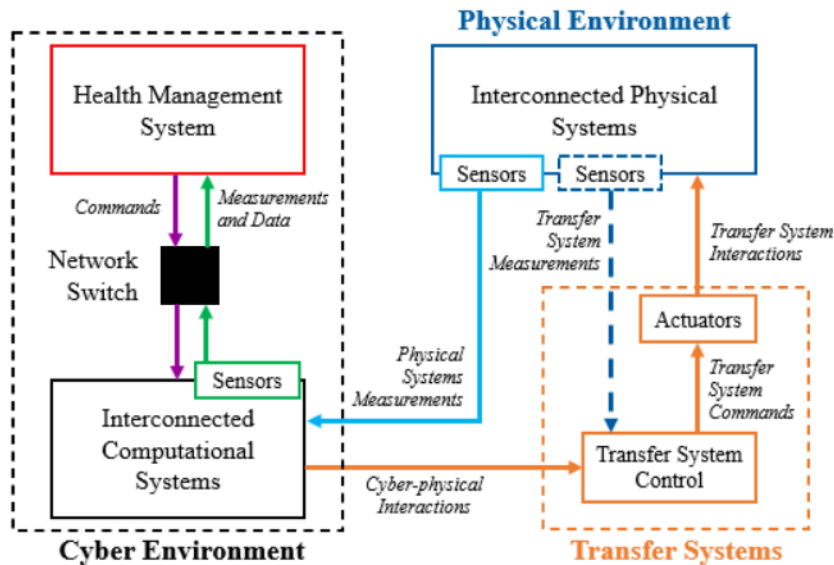


Figure 3-CPT flowchart for RETHi habitat resilience design (adapted from [12])

The goal of this research is to develop and validate a Habitat Interior Environment Model for MCVT to capture the temperature and pressure changes with time-varying inputs from other

subsystems and under different disturbance scenarios within the interior environment. HIEM then outputs temperature and pressure to other subsystems for further analysis. HIEM is a model within MCVT's Simulink system-of-systems and herein it is developed and verified using qualitative analysis and validated using experimental data. HIEM must consider the lunar atmosphere. There have been similar models used for terrestrial buildings; however, this deep-space application has added complexity that is taken into consideration such as extreme lunar temperatures, near-vacuum atmosphere, and other interactions with habitat subsystems previously mentioned. Before developing the HIEM model, several specific features and requirements for this model were identified to enable the entire MCVT to be integrated and thus simulate SmartHabs. Below are some of the significant requirements of the HIEM model:

- developed in Simulink for execution on Speedgoat real-time machine
- stable in all disruption scenarios
- compatible with other subsystems and the design structure matrix
- computationally efficient approach
- must be compatible with disturbances affecting HIEM
- must include an airlock
- account for latent and sensible loads, air leaks, pressure loss, ventilation, and recirculation
- temperature and pressure must be coupled

Chapter 2 details different models of temperature and pressure that were considered to aid in the development of the HIEM subsystem. Chapter 3 delves into the methodology of model development and its verification, followed by the experimental validation of the model in Chapter 4. Chapter 5 summarizes the results of the model under normal conditions and with disturbance scenarios.

## **2. LITERATURE REVIEW**

### **2.1 Thermal Modeling Inspiration**

Models are useful tools for representing various scenarios in real-world applications [13]. Such modeling comes with limitations in computation time and accuracy [14]. Numerous studies have been aimed at modeling the thermal interactions within buildings to monitor the effects on voltage network operations [15]. R.C. Johnson et al. [15] created a multi-zone residential UK building model to simulate the electrical demand of the structure over time. The Electrified Water and Space-heating Profiler uses thermal network equations to determine the thermal variations within these buildings throughout the day depending on human activities, weather, and building architecture [15]. The result is a streamlined, high-speed program that is user friendly with accurate results validated using real-world data [15]. Similarly, Zequn Wang et al. [14] developed a simplified RC model for house thermal dynamics to enhance building energy performance. Zequn Wang et al. simplified a complex RC model by eliminating non-identifiable parameters, or parameters that cannot be distinctively determined, to improve computation time [14]. Each floor is a thermal zone used in the thermal network calculation along with outdoor temperature, solar radiation, and heating power [14]. The model was able to accurately output the zonal temperatures faster than competing complex RC models [14].

### **2.2 Pressure Modeling Inspiration**

Modeling internal pressure is necessary in marine, air, space, and extreme weather applications [16,17]. Low interior pressures within constructions can result in catastrophic structural failure [17]. Severe winds cause pressure that apply various forces on structural elements [17]. When a structure is breached, the pressures enter the interior environment and apply additional forces on the structure that may lead to its demise [17]. Aaron L. Jaffe [17] created a model to predict the internal pressure of buildings in tornadic winds as compared to “straight-lined”—wind [17]. Jaffe used a dynamic pressure equation based on Bernoulli’s equation for an unsteady fluid flow along a streamline [17,18]. Jaffe also discusses a “slug of air” inspired by the Helmholtz resonator caused by fluid flow changes and resonance instability [17,19]. This air slug moves in and out of the opening between the external and internal pressures [19] and is treated as a spring-mass-damper system with a single degree of freedom [20]. Jaffe was able to accurately predict the interior

pressure of low-rise buildings in tornadic winds using the scientific methods described and validated using test data [17].

## **3. METHODOLOGY**

### **3.1. Model Description**

The Habitat Interior Environment Model developed herein is a physics-based one-dimensional Simulink model that delivers real-time information concerning the air temperature and pressure within the dome. HIEM accounts for various thermal and mass flow exchanges for thermal and pressure accuracy over time. The development of HIEM proceeded in three phases: the temperature model, pressure model, and coupling of the two through mass conservation and energy conservation. The temperature model uses thermal network calculations that include thermal resistances and heat transfer coefficients (explained in detail in **3.2**). The pressure model was created in a two-part manner. When there is no air leakage, pressure is calculated using the Ideal Gas Law. When there is air leakage, a dynamic pressure calculation is used. The temperature and pressure models were then coupled using a control volume analysis with mass and energy conservation in order to observe the changes in the two with different disturbances. HIEM also accounts for changes to the thermodynamic state of air that occur due to neighboring subsystems. ECLSS provides heating and cooling loads to alter temperature and supply and relief inputs to modify pressure. In this way, ECLSS can ensure that the interior environment is within an acceptable range. Similarly, the structural subsystem provides the wall temperature used for air temperature calculations. In turn, HIEM outputs necessary information to ECLSS, structures, and power subsystems for further analysis. This flow of inputs and outputs is depicted in Figure 4. Figure 5 shows the layer beneath Figure 2 for the interior environment model.

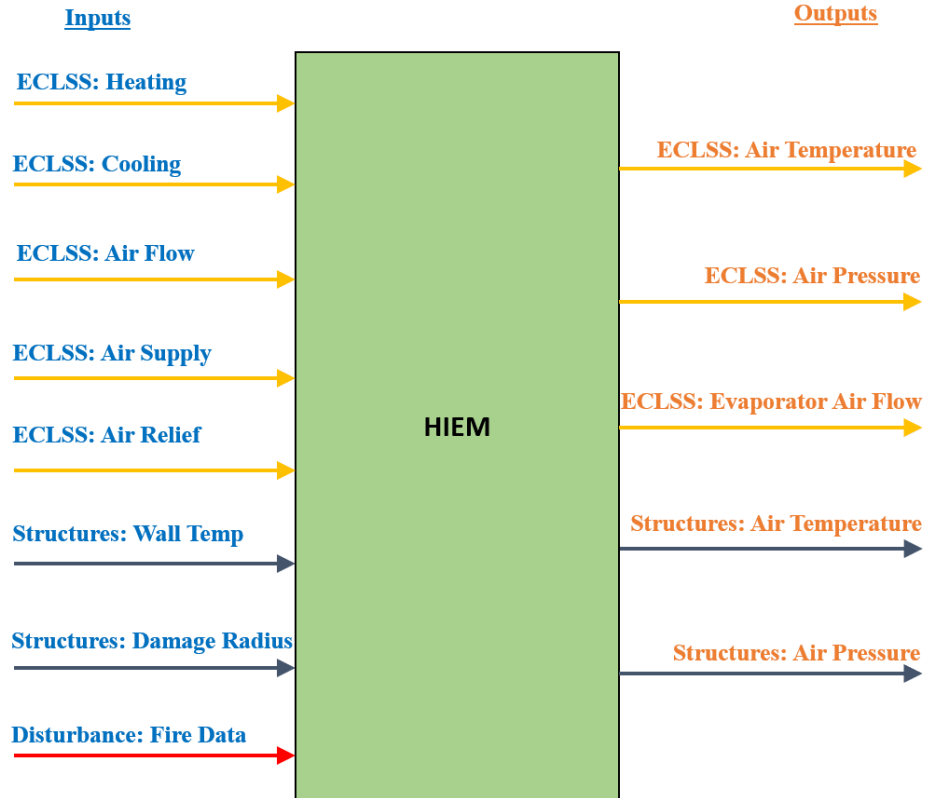


Figure 4-Depiction of HIEM inputs and outputs with neighboring subsystems



Figure 5-Simulink interior environment model

### **3.1.1 Habitat Interior Environment Model Disturbances**

To design a resilient habitat, disturbances are simulated to observe the effects of the extreme lunar environment. There are three main disturbances that affect the interior environment: fire, meteorite impact, and airlock failure. The disturbance model only sends information regarding fire and airlock failure directly to HEM. Meteorite impact disturbance information is sent to the structure subsystem which then outputs the radius size of the meteorite impact to HIEM. Each disturbance has an intensity level ranging from 1-5 that corresponds to a different disturbance description. An intensity level of 1 indicates that the habitat has no disturbance and is operating in normal conditions. An intensity level of 5 indicates that the disturbance will cause habitat failure. The next three sections describe the three disturbances affecting the interior environment in detail.

#### ***Fire***

Fire is the only disturbance considered in the MCVT disruption scenarios that starts within the interior environment. Fire intensity levels are established based on flame temperature [11]. Inherently, higher flame temperatures correlate to more dangerous scenarios. Flame temperatures are dependent upon the material being consumed. Only the materials expected to be in the habitat were analyzed for disturbance information [11]. Research has been conducted to observe the effects of fire in a microgravity environment [21]. It is worth noting that the maximum profile temperature of the flame in microgravity is similar to that of normal environmental conditions [11]. Table 3 shows the different fire intensity levels and their descriptions.

Table 3-Fire Disturbance Information [11]

Intensity Level	Flame Temp (°C)	Values	Description	Example
1	0	0cm	No fire within HIEM	Normal Operations
2	200-240	0.05cm	Localized fire with low thermal properties	Cotton, paper
3	275-615	0.015cm/sec	Fire with increasing radius	Plastic, polymer
4	600-900	0.067cm/sec	Fire with higher spread rate	Fire on electrical wires
5	1000-2500	3.5cm/sec	Fire with highest spread rate	Liquid fuel

For the purposes of the MCVT development, the team defined intensity levels as discrete numbers based on behavior and consequences. Fire with an intensity level 2 is defined as one in which there is a zero-spread rate. For example, this would be the case of a cotton ball on fire and burned up. Intensity level 3 would be more intense and might refer to a plastic table that catches fire and that fire spreads throughout the table. Intensity level 4 occurs when fire arises on an electrical cord. It is important to mention that in this scenario, the electrical wiring itself is not affected by the fire. Intensity level 5 indicates liquid fuel has caught fire and has the highest spread rate.

***Meteorite Impact***

Meteorite impact is another disruption. In this case, information is not directly given to the interior environment model. The disturbance model sends the information to other subsystems that it would directly affect, such as the structural subsystem. The structural subsystem then propagates information regarding the meteorite impact size when there is full penetration through the thickness of the habitat wall. When such an event occurs, a significant pressure drop is expected to occur within the interior environment. Full penetration occurs at intensity levels 4 and 5 indicating that these levels are the only meteorite impact intensities relevant for HIEM. Table 4 shows the different meteorite intensity levels.

Table 4-Meteorite Impact Disturbance Information [10]

Intensity	Description	Radius size (m)
-----------	-------------	-----------------

Level		
1	Normal Operations	0.000
2	Half penetration through structural protective layer (SPL)	0.000
3	Full penetration through SPL, no penetration through structural layer	0.000
4	Penetration through SPL and structural layer	0.005
5	Penetration through SPL and structural layer	0.008

### ***Airlock Failure***

An airlock is an essential aspect for structures in great pressure difference regions. They are used in space and marine applications for individuals to exit an earthly atmospheric environment to an environment with significant pressure variations and vice versa. In the airlock, individuals and equipment enter the chamber to slowly acclimate to the environment of which they are entering. It also protects the interior environment from losing its set pressure and temperature range when there is movement in and out of the habitat.

MCVT version 6.2 model does not include an actual airlock structure or zone. Instead, there is a place holder for an airlock failure scenario that acts as a very small air leakage to the exterior environment. However, an actual airlock zone has been modeled in a separate MCVT version that will be added into a future version of MCVT. Figure 6 shows a plan view of the two-dimensional model of the habitat with an airlock.

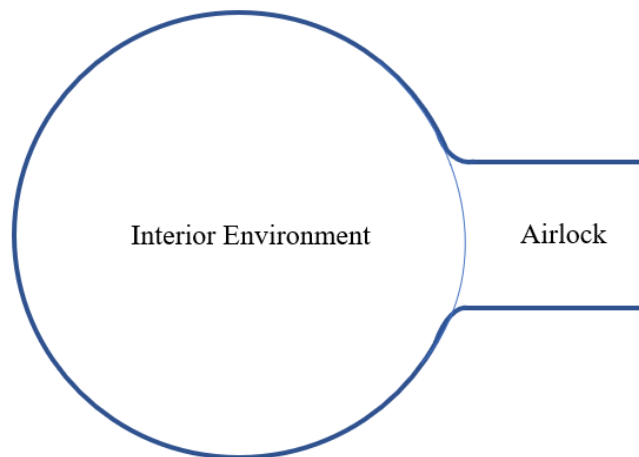


Figure 6-Simplified schematic showing the separation of the interior environment and airlock  
 Figure 7 visualizes the orientation of the inner and outer doors while Figure 8 depicts a rough 3D model of the habitat with an airlock.

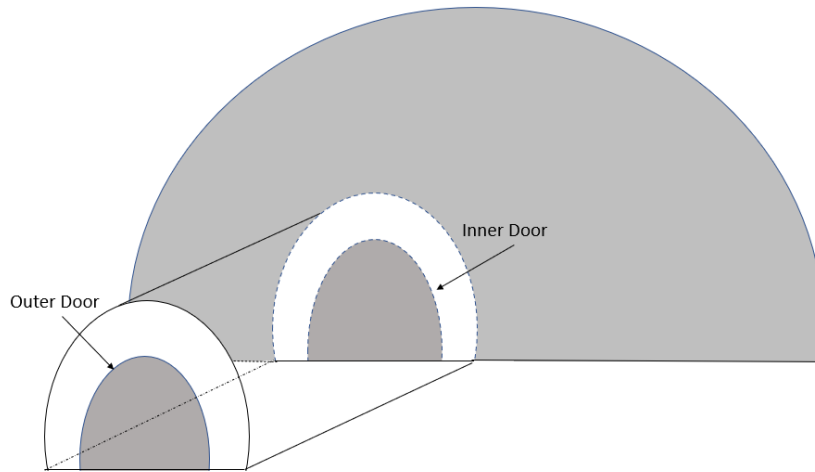


Figure 7-Drawing of the lunar habitat showing the inner and outer doors

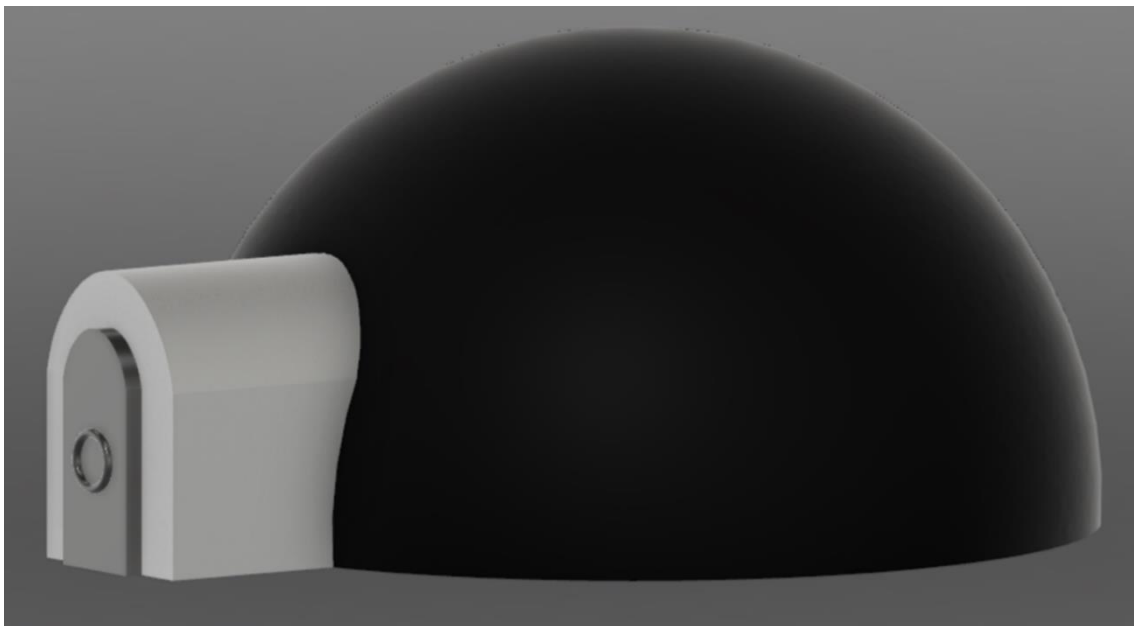


Figure 8-Conceptual 3D view of a lunar habitat with the addition of an airlock

The MCVT airlock is based on the Quest Joint Airlock used on the ISS. The airlock structure is modeled using a bladder, aluminum, insulation, and steel [22].

Due to the airlock not officially being a part of MCVT, only two failure scenarios are modeled as seen in Table 5.

Table 5-Airlock Failure Disturbance Information

Intensity Level	Description	Leakage radius size (m)
2	Inner door is open and there is a leakage from the outer door	0.002
3	Inner door is closed and there is a leakage between the airlock and interior environment	0.002

It is assumed that the airlock inner door will be open when not in use. In this case, the airlock failure will occur when the outer door has a leak (faulty gasket, not properly closed, obstruction, etc). When the inner door is closed, that means the airlock chamber is losing pressure. This failure will be modeled as the inner door failing due to a leak causing mass flow between the interior environment and the airlock zone.

### 3.2 Temperature Model

#### 3.2.1 Interior Environment Thermal Model

The interior environment temperature model was developed using a thermal network comprised of thermal resistances and thermal capacitances to account for energy flow throughout the system. The instantaneous energy flow reflects the thermal gains and losses (known as loads) that interact with the structure and therefore affects the zonal air temperature, internal structural mass, and exterior furnishings as seen in Figure 9.

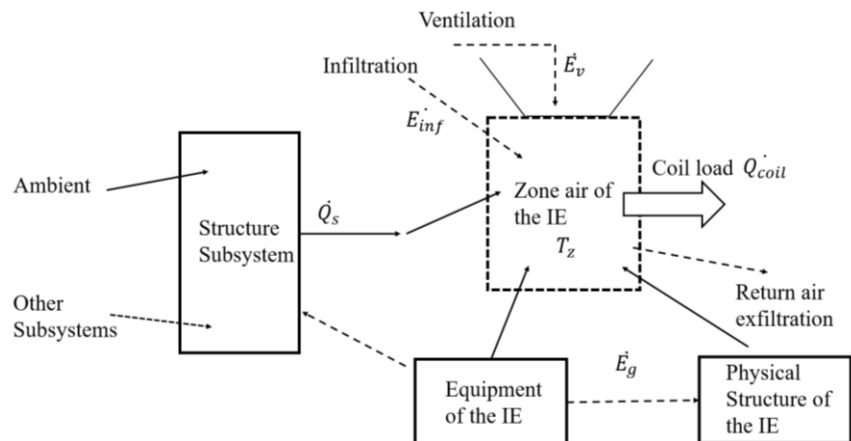


Figure 9-Interaction of gains and loads in the interior environment (adapted from [24])

Summation of these loads (gains and losses) are often out of phase with the instantaneous heat gain. Structural thermal storage delays the time at which radiative gains are integrated with the load. Furthermore, internal heat gains due to contents such as equipment, lights, and agent movement are considered and create variations of temperature within the lunar habitat throughout the day. Additionally, heat is transmitted to the interior surfaces of the structural subsystem. The structural interior surface transfers heat,  $\dot{Q}_s$ , via convection. The internal heat from equipment and individuals,  $\dot{E}_g$ , radiate heat within the zone and are transferred through convection from the internal mass to the zonal air. The zone's sensible energy flow (temperature change without phase change [23]) and latent energy flow (temperature change with phase change [23]) into the zone is controlled through ventilation,  $\dot{E}_v$ , and infiltration,  $\dot{E}_{inf}$ . The coil cooling load,  $\dot{Q}_{coil}$ , is the net heat that must be withdrawn to sustain a certain zone condition.

The ECLSS subsystem model has the capability to manage the temperature within the interior environment by supplying cooling and heating loads to keep the temperature within a comfortable range. When the temperature is higher than the upper bound of the setpoint range, ECLSS provides cooling until the temperature is once again within the proper range. When the temperature is lower than the lower bound of the setpoint range, ECLSS will then provide heating. These loads are determined using sensible energy. At the time this thesis is written, the humidity ratio has yet to be incorporated into the model. This model will be dependent on the moisture within the interior environment due to internal process and infiltration. When humidity is included, ECLSS will then have to adapt for the latent energy flow as well.

The gains and losses as they relate to cooling and heating are shown in Equation 1. In Equation 1,  $\dot{L}_T$  is the total load of the interior environment,  $\dot{Q}_s$  is the structural layer gains,  $\dot{E}_g$  is the internal gains,  $\dot{E}_v$  is the ventilation,  $\dot{E}_{inf}$  is the infiltration, and  $\frac{dE}{dt}$  is the energy storage.

$$\dot{L}_T = \dot{Q}_s + \dot{E}_g + \dot{E}_v + \dot{E}_{inf} - \frac{dE}{dt} \quad (Eqn. 1)$$

The heat balance method is used for the sensible cooling design to predict cooling and heating energy consumption for different scenarios and crew member configurations. The components included in the sensible cooling calculation to predict the sensible cooling load are shown in Figure 10. It is important to reiterate that the latent loads due to humidity are not included in the current

version of the model. When the habitat is occupied, heat gained from the occupants is added from the structure's surface. This heat gain is added directly to the zonal air through convection and in the interior mass. The heat gain that is added to the interior mass is stored and later transferred to the zonal air through convection.

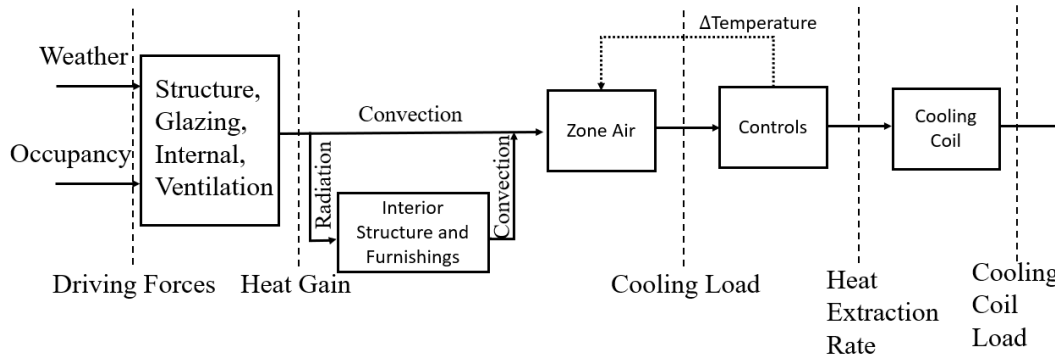


Figure 10-Sensible cooling calculation components (adapted from [24])

The zonal air energy balance equation is provided in Equation 2. It is assumed that the zone air is uniform throughout and negates the zonal air capacitance.  $\dot{Q}_{s,c}$  from the structure subsystem, the internal gains and thermal mass,  $\dot{Q}_{g,c}$ , and sensible energy from the ventilation airflow,  $\dot{E}_{v,s}$ , and infiltration,  $\dot{E}_{inf}$ . The energy flow is balanced by the sensible load,  $\dot{L}_s$ , from ECLSS. The instantaneous sensible heat balance for the zone is given in Equation 2.

$$\sum \dot{Q}_{s,c} + \sum \dot{Q}_{g,c} + \dot{L}_s + \dot{E}_{v,s} + \dot{E}_{inf} = 0 \quad (Eqn. 2)$$

Figure 11 visualizes the zone air heat balance.

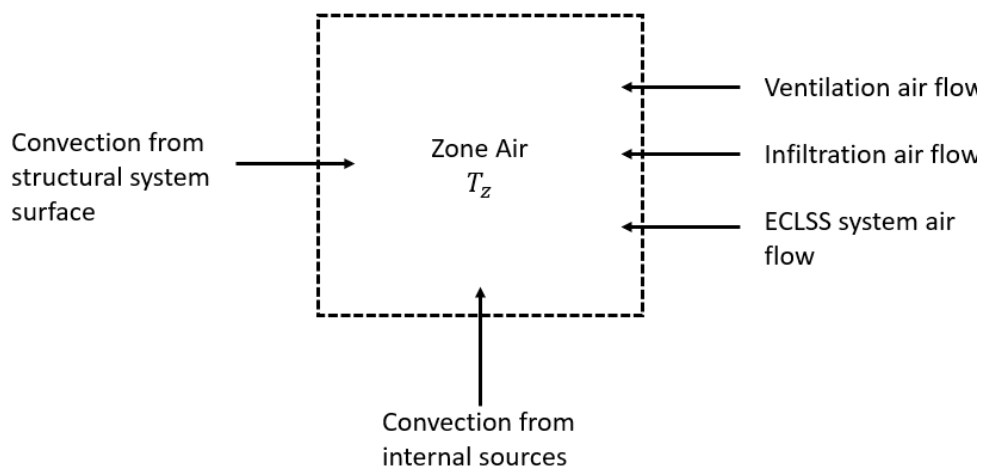


Figure 11- Zone air heat balance visualization (adapted from [24])

Figure 12 shows the thermal network used for the heat balance and radiant time series method from Figure 9. The thermal capacitance is represented as a lumped capacitance for the structure and furnishings. Furthermore, to simplify calculations, rather than analyzing the radiant exchanges, the radiant time series method is implemented to separate the radiant portion from the convection portion.

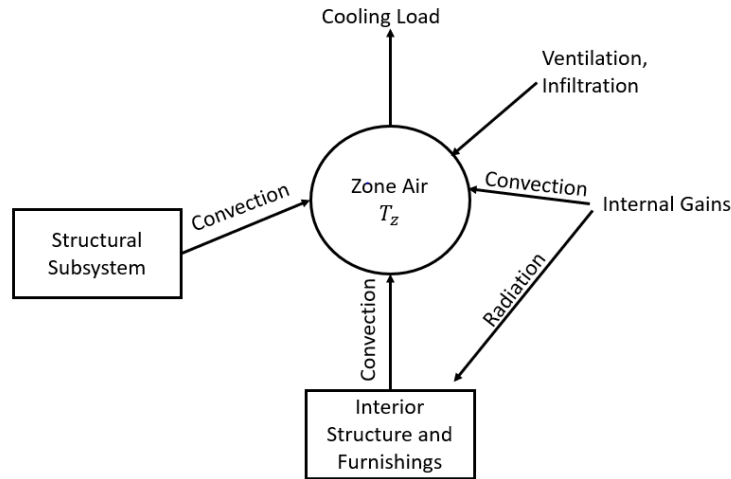


Figure 12-Heat flows for the thermal network (adapted from [24])

The thermal network approach involves thermal resistances and thermal capacitances to represent the heat flow into the zone from the structural layer. Figure 13 shows the thermal circuit for a zone with a single exterior wall.

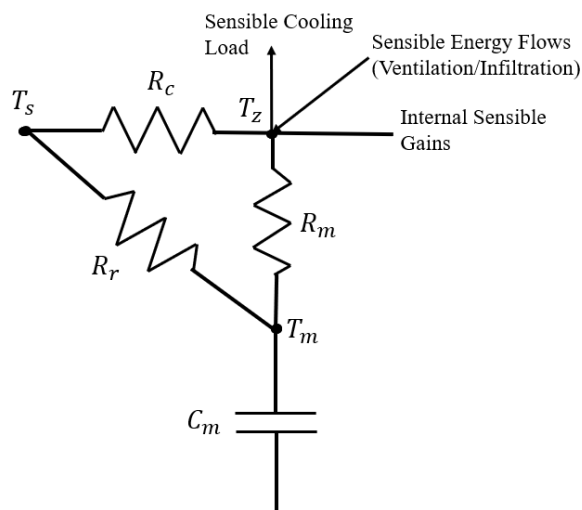


Figure 13- Thermal network of a single zone cooling load

In Figure 13,  $T_z$  is the temperature of the zone air,  $T_m$  is the temperature of the internal mass,  $T_s$  is the temperature of the structural layer,  $R_c$  is the thermal resistance of the wall,  $R_m$  is the thermal resistance of the internal mass convection,  $R_r$  is the thermal resistance of the internal mass radiation, and  $C_m$  is the thermal capacitance of the internal mass.  $T_z$  and  $T_s$  are both assumed to be constant, and the capacitor in the circuit represents the single external wall. The heat gain from the structure is transferred by convection to  $T_z$  and by radiation to  $T_m$ . The coefficient for the interior surfaces is comprised of convection and radiation coefficients used for respective convection and radiation transfers. The internal sensible gains generated by equipment and individuals and the glazing conductive gains are divided into a convective and a radiative fraction. These fractions cause a difference in temperature between the zonal air and internal mass resulting in convection transferring heat to the zone air.

Following this thermal network method, the temperature of the interior environment can then be found using the thermal network in Figure 14.

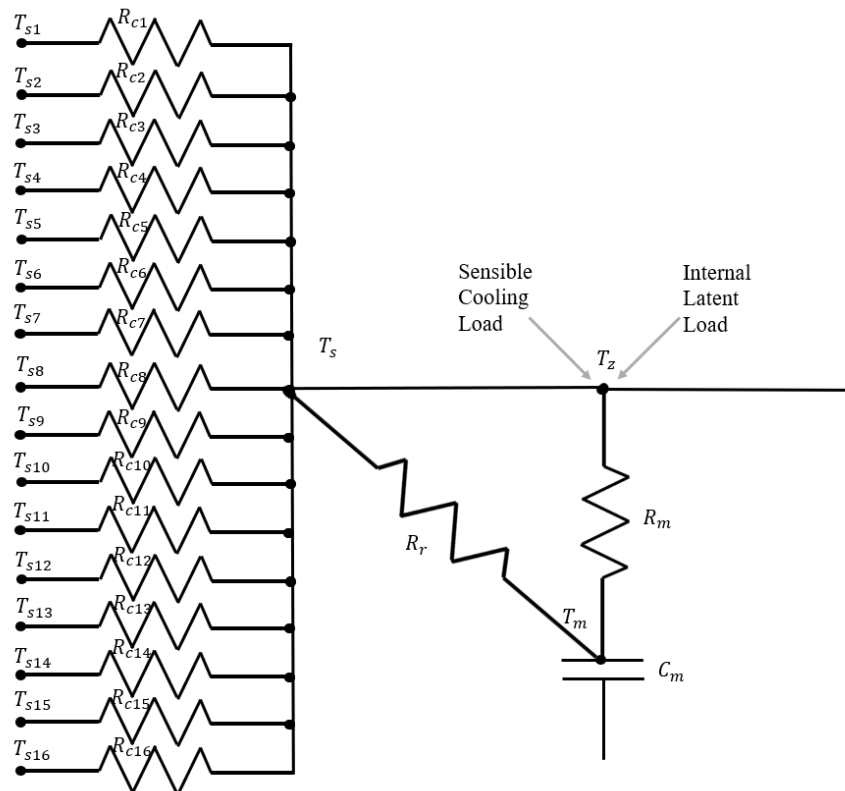


Figure 14-Thermal network for the interior environment

The sixteen temperature nodes on the left of Figure 14 are provided as inputs by the structural subsystem as the interior wall temperature. For MCVT modeling consistency, the interior environment and the structural subsystem teams agreed on these sixteen thermal panel nodes and their location to ease computation time and for mutual understanding of each subsystem behavior. Figure 15 below shows a plan view of the corresponding 2D location of the nodes located on the interior structural walls.

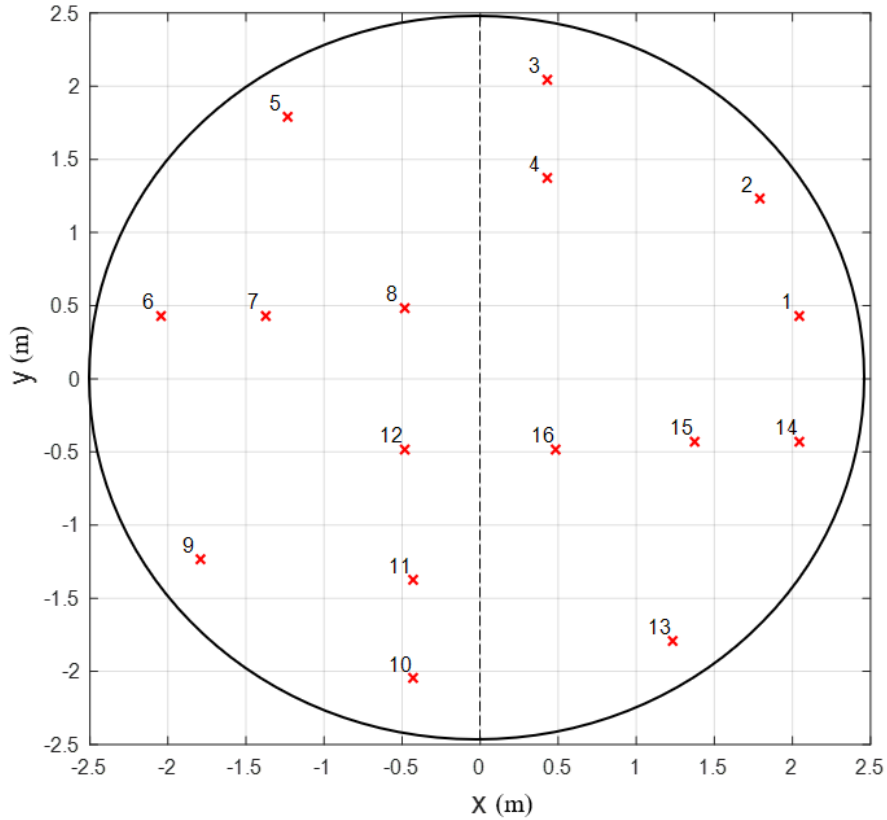


Figure 15- Structural subsystem nodal locations

The equations used for the thermal network in Figure 14 are provided below in Equations 3 and 4.

$$\frac{dT_m}{dt} = \frac{T_m - T_z}{R_m C_m} + \frac{T_s - T_m}{R_r C_m} + \frac{\sum F_{g,r} Q_g}{C_m} \quad (\text{Eqn. 3})$$

$$\begin{aligned}
& \frac{T_{s1} - T_z}{R_{c1}} + \frac{T_{s2} - T_z}{R_{c2}} + \frac{T_{s3} - T_z}{R_{c3}} + \frac{T_{s4} - T_z}{R_{c4}} + \frac{T_{s5} - T_z}{R_{c5}} + \frac{T_{s6} - T_z}{R_{c6}} + \frac{T_{s7} - T_z}{R_{c7}} + \frac{T_{s8} - T_z}{R_{c8}} \\
& + \frac{T_{s9} - T_z}{R_{c9}} + \frac{T_{s10} - T_z}{R_{c10}} + \frac{T_{s11} - T_z}{R_{c11}} + \frac{T_{s12} - T_z}{R_{c12}} + \frac{T_{s13} - T_z}{R_{c13}} + \frac{T_{s14} - T_z}{R_{c14}} + \frac{T_{s15} - T_z}{R_{c15}} \\
& + \frac{T_{s16} - T_z}{R_{c16}} + \frac{T_m - T_z}{R_m} + \sum F_{g,c} Q_g + Q_{cooling} \\
& = 0 \tag{Eqn. 4}
\end{aligned}$$

Equation 3 is a differential equation representing the temperature of the internal mass over time,  $\frac{dT_m}{dt}$ , as a function of the interior environment temperature,  $T_z$ , internal mass resistance,  $R_m$ , unit thermal capacitance,  $C_m$ , fraction of radiation,  $F_{g,r}$ , and internal gains,  $Q_g$ .

Equation 4 is the energy balance equation for Figure 14 using the sixteen nodes on the interior wall given by the structural subsystem from Figure 15. The numerical subscript represents the node at which that value is designated.

Table 6 reveals the parameter values used in Equations 3 and 4 to calculate the air temperature within the interior environment. Normally, RC models are calibrated using experimental data for respective resistance and capacitance values. For MCVT, representative values are used to predict the thermodynamics of the system. The thermal capacitance of the internal mass is a significant variable in predicting such dynamics since it affects the zone's thermal response.

Table 6-Thermal resistance and unit thermal capacitance values

Parameter	Value
Thermal resistance for convection, $R_{cn}$	0.325 hr-ft <sup>2</sup> -°F/Btu
Thermal resistance for internal mass, $R_m$	1.68 hr-ft <sup>2</sup> -°F/Btu
Unit thermal capacitance, $C_m$	10 Btu/ ft <sup>2</sup> -°F

Furthermore, the radiative and convective fractions are provided in Table 7. Since the radiative fractions are generally double that of convective fractions, the radiant heat transfer from a wall surface to internal mass is roughly double the convective heat transfer from surface to air. The internal gains,  $Q_g$ , are calculated using the radiative and convective fractions as shown in Table 8.

Table 7-Radiative and convective fraction values

Source of Heat Flow	Radiative Fraction	Convective Fraction
Occupants	0.6	0.4
Walls	0.63	0.37
Equipment	0.1-0.4	0.6-0.9
Incandescent Lighting	0.8	0.2

Table 8-Internal gains values

Symbol	Illumination Gain	People Sensible Gain	Equipment Sensible Gain
$F_{g,r}$	0.33	0.3	0.5
$F_{g,c}$	0.67	0.7	0.5
$Q_g$	$Q_{lights}$ $= 3.07I_{occ}A_{floor}$ Btu/hr	$Q_{people} = 245I_{occ}$ Btu/hr	$Q_{people} = 400I_{occ}$ Btu/hr

### Fire Calculation

During a fire disruption scenario, the interior environment receives a fire radius from the disturbance block in Simulink. This fire radius is then used to calculate the appropriate heat release rate of the fire at the specified intensity level being considered, as discussed in Section 3.1.1 using Equation 5 [25]:

$$\dot{Q}_{fire} = \chi\alpha_1\alpha_2A\sqrt{h} \quad (Eqn. 5)$$

where  $\chi$  is the combustion efficiency,  $\alpha_1$  is the flow constant ( $\frac{kg}{s*m^{5/2}}$ ),  $\alpha_2$  is the combustion energy developed per unit mass of air constant ( $\frac{W*s}{kg}$ ), A is the area of the fire ( $m^2$ ), and h is the height of the fire (m). Table 9 shows the values used for  $\chi$ ,  $\alpha_1$ , and  $\alpha_2$  at different intensity levels.

Table 9-Fire calculation values

Fire Intensity Level	$\chi$	$\alpha_1 \left( \frac{kg}{s * m^{5/2}} \right)$	$\alpha_2 \left( \frac{W * s}{kg} \right)$
2	0.60	0.05	$1.8 \cdot 10^6$
3	0.70	0.05	$2.0 \cdot 10^6$
4	0.83	0.05	$2.2 \cdot 10^6$
5	0.93	0.05	$3.0 \cdot 10^6$

### 3.2.2 Airlock Thermal Model

Modeling the airlock thermal model is very similar to that of the interior environment. The airlock thermal network is seen below in Figure 16 based on the airlock structure (bladder, aluminum, insulation, and steel).

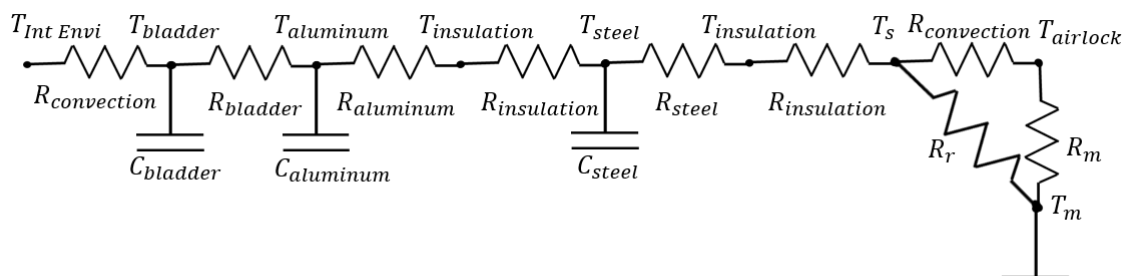


Figure 16-Airlock thermal network

The resulting energy balance equation is then:

$$\frac{T_{steel} - T_s}{R_{out}} + \frac{T_m - T_s}{R_r} + \frac{T_{Int Envi} - T_s}{R_c} = 0 \quad (Eqn. 6)$$

where  $T_{steel}$  is the temperature of the steel,  $T_{Int Envi}$  is the temperature of the interior environment,  $T_m$  is the temperature of the internal mass,  $T_s$  is the interior surface temperature of the airlock,  $R_c$  is the thermal resistance of the wall,  $R_r$  is the thermal resistance of the internal mass radiation ( $R_{out}$ ).

The energy balance equations regarding  $T_s$  are seen below.

$$\frac{T_{insulation} - T_s}{R_{insulation}} + \frac{T_{airlock} - T_s}{R_{convection}} + \frac{T_m - T_s}{R_r} = 0 \quad (Eqn. 7)$$

$$\frac{T_s - T_{airlock}}{R_{convection}} + \frac{T_m - T_{airlock}}{R_m} + \dot{Q}_{cooling} + \sum F_{g,c} Q_g = 0 \quad (Eqn. 8)$$

The last term in Equation 8 is the internal gains due to convection. Additionally, the energy balance equations due to the effect of the insulation are seen here.

$$\frac{T_{aluminum} - T_{insulation}}{R_{aluminum}} + \frac{T_{steel} - T_{insulation}}{R_{insulation}} = 0 \quad (Eqn. 9)$$

$$\frac{T_{steel} - T_{insulation}}{R_{steel}} + \frac{T_s - T_{insulation}}{R_{insulation}} = 0 \quad (Eqn. 10)$$

Since there is no input from the structural subsystem regarding the wall temperature of the airlock, a thermal resistance network consisting of the materials of the airlock structure is developed. The following equations are the differential equations pertaining to the temperature of each material as a function of time based on Figure 16.

$$\frac{dT_{bladder}}{dt} = \left( \frac{T_{Int Envi} - T_{bladder}}{R_{convection} C_{bladder}} \right) + \left( \frac{T_{aluminum} - T_{bladder}}{R_{bladder} C_{bladder}} \right) \quad (Eqn. 11)$$

$$\frac{dT_{aluminum}}{dt} = \left( \frac{T_{bladder} - T_{aluminum}}{R_{bladder} C_{aluminum}} \right) + \left( \frac{T_{insulation} - T_{aluminum}}{R_{aluminum} C_{aluminum}} \right) \quad (Eqn. 12)$$

$$\frac{dT_{steel}}{dt} = \left( \frac{T_{insulation} - T_{steel}}{R_{insulation} C_{steel}} \right) + \left( \frac{T_{insulation} - T_{steel}}{R_{insulation} C_{steel}} \right) \quad (Eqn. 13)$$

$$\frac{dT_m}{dt} = \left( \frac{T_{airlock} - T_m}{R_m C_m} \right) + \left( \frac{T_s - T_m}{R_r C_m} \right) + \frac{\sum F_{g,r} Q_g}{C_m} = 0 \quad (Eqn. 14)$$

The last term in Equation 14 is the internal gains due to radiation.

### 3.2.3 Natural Convection Between Interior Environment and Airlock

When the inner door of the airlock is open, there is convection occurring between the airlock chamber and the interior environment. To calculate the air convection between the two, Equation 15 is adopted.

$$\dot{Q}_{conv,zones} = h * A_y * (T_{Int Envi} - T_{airlock}) \quad (Eqn. 15)$$

In Equation 15,  $\dot{Q}_{conv,zones}$  is the convection between the zones ( $W$ ),  $h$  is the enthalpy of the air ( $kJ/kg$ ), and  $A_y$  is the y-axis area separating the airlock and interior environment ( $m^2$ ). When the inner door is open,  $\dot{Q}_{conv,zones}$  is summed with the other calculated heat transfer values—convection from the walls, fire, and thermal load—to generate a  $\dot{Q}_{cv}$  value from Equation 29 that is included in the coupling process as explained in Section 3.4.

The air enthalpy used in Equation 16 is found using the Nusselt number (Equation 17). The Nusselt number is the ratio of heat transfer by convection and conduction [26]. This ratio can be correlated to the Rayleigh number for a fluid's natural convection [26]. Equation 18 shows the equation of the Rayleigh number as a product of the Grashof number (Equation 19) and Prandtl (Equation 20). The Grashof number is an approximate ratio of buoyancy to viscous forces on a fluid while the Prandtl number is the ratio of momentum diffusivity and thermal diffusivity.

$$h = \frac{Nu * k_{air}}{L} \quad (Eqn. 16)$$

$$Nu = 0.26 * Ra^{1/3} \quad (Eqn. 17)$$

$$Ra = Gr * Pr \quad (Eqn. 18)$$

$$Gr = \frac{L^3 * \rho_{air}^2 * g * \Delta T * \alpha_{air}}{\nu_{air}} \quad (Eqn. 19)$$

$$Pr = \frac{\nu_{air} * c_{v,air}}{k_{air}} \quad (Eqn. 20)$$

In Equations 16-20,  $k_{air}$  is the thermal conductivity of air ( $W/m - K$ ),  $L$  is the characteristic length ( $m$ ),  $\rho_{air}$  is the density of air ( $kg/m^3$ ),  $g$  is the gravitational acceleration of the moon ( $m/s^2$ ),  $\Delta T$  is the difference of temperatures ( $K$ ),  $\alpha_{air}$  is the thermal expansion coefficient,  $\nu_{air}$  is viscosity of the air ( $N - s/m^2$ ).

### 3.3 Pressure Model

#### 3.2.1 Interior Environment Pressure Model

When there are no disruptions, the interior environment pressure,  $P$ , is measured in Pascal's using the ideal gas equation below.

$$P = \frac{m}{MM} \frac{\bar{R}T}{V} \quad (Eqn. 21)$$

In Equation 21,  $m$  is the mass of air ( $g$ ),  $MM$  is the molar mass of air ( $gmol^{-1}$ ),  $\bar{R}$  is the universal gas constant ( $K^{-1}mol^{-1}$ ),  $T$  is the interior environment temperature ( $K$ ), and  $V$  is the volume of the interior environment ( $m^3$ ).

When there is a fire disturbance, Equation 21 is also used to calculate the pressure of the interior environment. Such variations in pressure are correspondingly seen through the direct relationship with temperature.

### 3.2.2 Meteorite Air Leakage Pressure Model

In the event of a meteorite impact or other pressure leakage scenario, pressure variations are calculated using the modeling approach adopted from Jaffe [17]. This method was developed to predict the pressure fluctuations inside low-rise buildings with single or multiple openings during a tornado and was inspired by Jeong Hee Oh [17]. The equation used to model this dynamic pressure is derived from Bernoulli's equation for an unsteady fluid along a streamline is given below in Equation 22. The equation assumes that the fluid is incompressible, inviscid, and isothermal.

$$\rho \int_1^2 \frac{\partial U}{\partial t} ds + \int_1^2 dp + \int_1^2 \frac{1}{2} \rho (U_2^2 - U_1^2) + \rho g (z_2 - z_1) = 0 \quad (\text{Eqn. 22})$$

In Equation 22,  $\rho$  is the fluid density,  $U$  is the flow velocity,  $p$  is the fluid's pressure,  $g$  is gravitational acceleration, and  $z$  is the height [18]. The first term represents the unsteady term, the second term is the change in flow pressure energy, the third term is the change in velocity, and the fourth term is the change in height [18].

At an opening in the structure, the internal pressure and external pressures meet. Here there is a "slug of air" that moves in and out [27] as depicted in Figure 17. This concept stems from the Helmholtz resonator, fluid flow change, and resonance instability. It can be assumed that there is no net flow of the air slug and that the interior pressure is uniform. It is also worth noting that these slugs have been observed in microgravity conditions [27]; therefore, it is applicable to continue using this calculation method to determine the pressure of the interior environment in cases of air leakages.

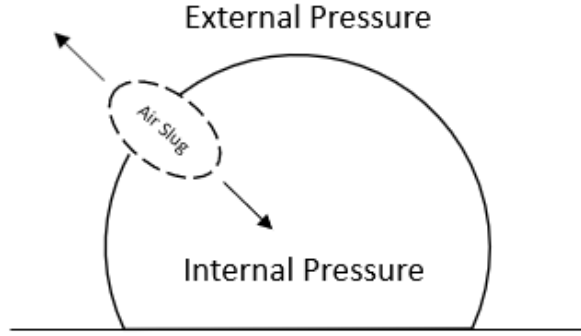


Figure 17-Air slug in lunar habitat opening

Coupling the concept of Bernoulli's equation with the notion of an air slug creates a single degree of freedom mass-spring damping system as shown in Equation 23 [17]. In this system equation, the air slug is treated as the mass.

$$\rho l_e \ddot{x} + C_L \rho \frac{\dot{x}|\dot{x}|}{2} = P_e - P_i \quad (\text{Eqn. 23})$$

In the equation,  $\rho$  is the density of air ( $\text{kg/m}^3$ ),  $l_e$  is effective length of air slug (m),  $C_L$  is the loss coefficient through the opening,  $P_e$  is the external pressure (Pa),  $P_i$  is the internal pressure (Pa),  $\ddot{x}$  is the acceleration of the air slug ( $\text{m/s}^2$ ), and  $\dot{x}$  is the air slug velocity (m/s).

Further adaptation of Equation 23 leads to Equation 24 for a single discharge or a single meteorite hit with full penetration [17]. Multiple meteorite impact analyses will be studied in later versions of the model.

$$\frac{\rho l_e V_o}{\gamma A P_o} \ddot{P}_i^j + \frac{C_L \rho V_o^2}{2 \gamma^2 A^2 P_o^2} \dot{P}_i^j | \dot{P}_i^j | + P_i^j = P_e^j \quad (\text{Eqn. 24})$$

where  $\rho$  is the density of air ( $\text{kg/m}^3$ ),  $l_e$  is effective length of air slug (m),  $V_o$  internal volume of building ( $\text{m}^3$ ),  $\gamma$  is the ratio of specific heat of air,  $A$  is the area of the opening ( $\text{m}^2$ ),  $P_o$  is static pressure (Pa),  $C_L$  is the loss coefficient through the opening,  $\ddot{P}_i^j$  is the second time derivative of internal pressure ( $\text{Pa}^3$ ),  $\dot{P}_i^j$  is the  $j^{\text{th}}$  time derivative of internal pressure ( $\text{Pa}^2$ ),  $P_i^j$  is the internal pressure (Pa), and  $P_e^j$  is  $j^{\text{th}}$  time step of the external pressure or the moon's atmospheric pressure (Pa). The values for these parameters are shown in Table 10.

Table 10-Dynamic pressure values

$\rho$	$V_0$	$\gamma$	$P_o$	$C_l$	$l_0$	$P_e^j$
$1.23 \text{ kg/m}^3$	$32 \text{ m}^3$	1.4	$10^5 \text{ Pa}$	2.5	0.6 m	$3 \times 10^{-10} \text{ Pa}$

The area of the opening is assumed to be circular and is calculated using the value of the radius provided by the structural team. The effective length of air slug,  $l_e$ , is calculated in meters using Equation 25, where  $l_0$  is the structural wall thickness:

$$l_e = l_0 + 0.89\sqrt{A} \quad (\text{Eqn. 25})$$

The loss coefficient is included to account for losses including frictional and acceleration components. However, a reference value of 2.5 [18] is used here, although it for terrestrial applications and will need to be appropriately changed to reflect deep space habitat designs.

Using the variables in Table 10, Equations 24 and 25, disturbance inputs, and Simulink, it is possible to switch between the correct pressure calculations at each time step. If a meteorite impact or air leakage occurs, Simulink can solve the differential equation (Equation 24) for the internal pressure during each time step using the Ideal Gas equation as an initial condition.

The pressure model then needs to be coupled with the temperature model as will be discussed in Section 3.4. In order to do this for dynamic pressure changes, the dynamic pressure model goes through another calculation as seen in Equation 6 to calculate the mass flow leaving the interior environment. This mass flow is accounted for in the coupling process to observe the effects of temperature with decreasing pressure.

$$\dot{m} = c_d * A * \sqrt{2 * \rho * (P_1 - P_2)} \quad (\text{Eqn. 26})$$

In Equation 26,  $\dot{m}$  is the mass flow rate leaving the interior environment ( $kg/s$ ),  $c_d$  is the discharge coefficient,  $A$  is the area of the opening ( $m$ ),  $P_1$  is the pressure of the interior environment (Pa),  $P_2$  is the lunar atmospheric pressure (Pa), and  $\rho$  is the density of the air in the interior environment ( $kg/m^3$ ). The mass flow equation stems from Bernoulli's equation and the continuity equation assuming steady-state, incompressible, inviscid, and laminar flow.

It is important to note that in Equations 24 and 26 there are two coefficients,  $C_l$  and  $c_d$ , that need to be calibrated through testing in order to accurately calculate pressure changes for system specific

fluid flows. For the results in Chapter 5, a  $C_L$  value of 2.5 and a  $c_d$  value of 0.6 are used. Chapter 4 uses test data to estimate these values in relation to the pressure box used in CPT.

### 3.3 Coupling Pressure and Temperature

The temperature and pressure models are coupled using energy balance equations rather than using tabulated capacitance values [28]. The node represents the lumped air is replaced by a more elaborated formulation to account for the two-way coupling between temperature and pressure. The control volume is constrained by the inner surfaces of the lunar habitat and is used for the conservation of mass and energy. This concept is used to develop the coupling method seen below using an open control volume analysis [29].

The equation for conservation of mass (Equation 27):

$$\frac{dm_{cv}}{dt} = \sum_i \dot{m}_i - \sum_e \dot{m}_e \quad (\text{Eqn. 27})$$

where  $m_{cv}$  is the control volume mass of the air ( $kg$ ),  $\dot{m}_i$  in the mass flow rate of air entering the control boundary ( $kg/s$ ), and  $\dot{m}_e$  is the exiting mass flow rate crossing the boundary of the constant control volume ( $kg/s$ ). Then, the mass of the interior habitat is strictly a function of density, resulting in the simplification:

$$V_{cv} \frac{d\rho}{dt} = \sum_i \dot{m}_i - \sum_e \dot{m}_e \quad (\text{Eqn. 28})$$

where  $V_{cv}$  is the volume of the air ( $m^3$ ), and  $\frac{d\rho}{dt}$  is the change of air density with respect to time.

The equation for the conservation of energy is:

$$\begin{aligned} \frac{dE_{cv}}{dt} = & \dot{Q}_{cv} - \dot{W}_{cv} + \sum_i \dot{m}_i \left( h_i + \frac{v_i^2}{2} + gz_i \right) \\ & - \sum_e \dot{m}_e \left( h_e + \frac{v_e^2}{2} + gz_e \right) \end{aligned} \quad (\text{Eqn. 29})$$

where  $E_{cv}$  is the energy in the control volume ( $W$ ),  $\dot{Q}_{cv}$  is the heat transfer rate added to the control volume ( $W$ ),  $\dot{W}_{cv}$  is the rate of the boundary work done ( $W$ ),  $h$  is the specific enthalpy of the air ( $kg/s$ ),  $v$  is the mean velocity of air ( $m/s$ ),  $g$  is the gravitational acceleration ( $m/s^2$ ), and  $z$  is the

height at which mass transfer through the boundary occurs ( $m$ ) [30]. Subscripts  $i$  and  $e$  indicate whether the properties are for entering or exiting the control volume, respectively. This base formulation can be further simplified by assuming the kinetic energy, potential energy, and boundary work terms are negligible. Furthermore, a constant control volume assumption is made for the mass conservation equation. The resulting equation is seen below in Equation 30.

$$V_{cv} \frac{d(\rho u)}{dt} = \dot{Q}_{cv} + \dot{m}_i h_i + \dot{m}_e h_e \quad (\text{Eqn. 30})$$

In Equation 30,  $u$  is the internal energy of the air ( $kJ/kg - K$ ). For the simplicity of conveying the derivations, a control volume with only one inlet and outlet will be considered.

Taking inspiration from Equations 29 and 30, where the authors reorganized the energy and mass conservation laws to be specific to specific enthalpy and pressure for a gas tank pressurization and heat exchanger modeling. A similar approach can be adapted by using the fact that

$$\frac{d\rho}{dt} = \left(\frac{\partial\rho}{\partial h}\right)_p \frac{dh}{dt} + \left(\frac{\partial\rho}{\partial P}\right)_h \frac{dP}{dt} \quad (\text{Eqn. 31})$$

density is a function of two intensive thermodynamic properties—specific enthalpy and pressure. The left-hand-side of Equation 30 can then be rearranged to be explicit in enthalpy and pressure as below:

$$LHS\ of\ (30) = V_{cv} \frac{d(\rho u)}{dt} = V_{cv} \frac{d(\rho h - P)}{dt} = V_{cv} \left( \rho \frac{\partial h}{\partial t} + h \frac{\partial \rho}{\partial t} - \frac{\partial P}{\partial t} \right) \quad (\text{Eqn. 32})$$

and this equation is combined with the relationship described in Equation 31 to produce the final expression of the conservation of energy explicit in enthalpy and pressure. The resulting expression is:

$$V_{cv} \left[ \rho + h \left(\frac{\partial\rho}{\partial h}\right)_p \right] \frac{dh}{dt} + V_{cv} \left[ h \left(\frac{\partial\rho}{\partial P}\right)_h - 1 \right] \frac{dP}{dt} = \dot{Q}_{cv} + \dot{m}_i h_i - \dot{m}_e h_e \quad (\text{Eqn. 33})$$

where the partial derivatives are to be numerically obtained by employing tabulated thermodynamic properties [31] or by implemented equations of state (e.g., ideal gas law relationship). Similarly, the conservation of energy, the conservation of mass expression, and Equation 28 can be written in terms of enthalpy and pressure as below:

$$V_{cv} \left(\frac{\partial\rho}{\partial h}\right)_p \frac{dh}{dt} + V_{cv} \left(\frac{\partial\rho}{\partial P}\right)_h \frac{dP}{dt} = \dot{m}_i - \dot{m}_e \quad (\text{Eqn. 34})$$

The two resulting equations, Equations 33 and 34, are to be solved simultaneously at each timestep during the simulation.

Within the context of integration of the new air model with rest of the thermal resistance network and the air slug model, the outputs of the models, total heat transfer rate and total mass transfer rate, can be used to be the inputs to the interior air model described above. Practically, these values would be the terms on the right-hand-side of the two equations above. With appropriate timestep values, the integration of these three models will result in reliable and robust behavior estimation of the interior environment. As a concluding remark, the formulation can be readily extended to humid air calculations by using homogeneous humid air properties or a multi-parameter equation of state of air as a mixture [32]. A mass conservation equation for water vapor can also be included.

Using the MATLAB's C++ library, CoolProp, would be an easier method to implement for the coupling process as it has fluid and thermodynamic properties [31]; however, doing so would require the entirety of RETHi's to learn and install the program to run the whole MCVT model. This would be a time-consuming process and possibly subject to more errors with inexperienced users, so the HIEM team decided it was best to use the aforementioned coupling process instead of using CoolProp.

## 4. HIEM MODEL VALIDATION USING CPT MODEL

### 4.1 Experimental Setup

To validate the MCVT HIEM model, a fabricated and insulated steel pressure box is used to obtain experimental data under several pressure leakage scenarios. The pressure box is shown in Figure 18 with dimensions in Appendix B.



Figure 18-Pressure box

The hardware, sensors, and insulation used for the pressure box is seen in Table 11 [33].

Table 11-List of sensors and hardware used [33]

Equipment	Manufacturer	Model
Thermocouple	Industrial Process and Sensor Omega (Feedthroughs)	T-20-TPFT2NPT-4T
Thermocouple probe	Industrial Process and Sensor	TG20T0142U00600MP
Flow meter	Hoffer	HO1/2X1/4A-.35-3.5-BP-1MX- MS-X
Pressure transducer	Omega	PX309-050A10V
Thermocouple module	National Instrument	NI-9213
Target machine	Speedgoat	Performance real-time target machine
Insulation	Foamular 250	R-7.5-270815

The experiment was conducted by increasing the pressure of the pressure box to approximately 15psi. This condition is used to start each experiment. After recording the external temperature and pressure prior to the start of each test, the data acquisition system was initiated, and a command is sent from MATLAB to the mass flow controller. The command is initially 0 Volts, but then a step change after 15 seconds activates a 1, 2, or 3 Volts for a duration of 200 seconds. A sample of the signal sent to the mass flow controller from MATLAB is shown in Figure 19.

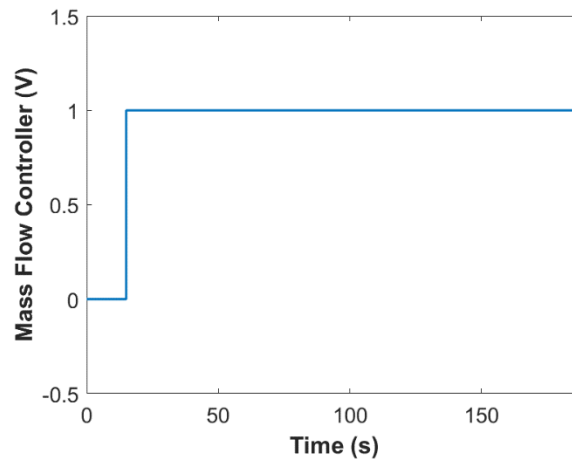


Figure 19-Sample signal sent to mass flow controller

The thermocouples in the pressure box were used to measure the temperature, the pressure sensors were used to record the pressure, and the mass flow rate readings were recorded. All the data collected were then converted from Volts to the corresponding engineering units. There was significant noise in the data due to electrical connections and electrical interference. The noise was filtered using the “movemean” command in MATLAB for further calculations. Figure 20 shows a sample of the data before and after filtering the noise.

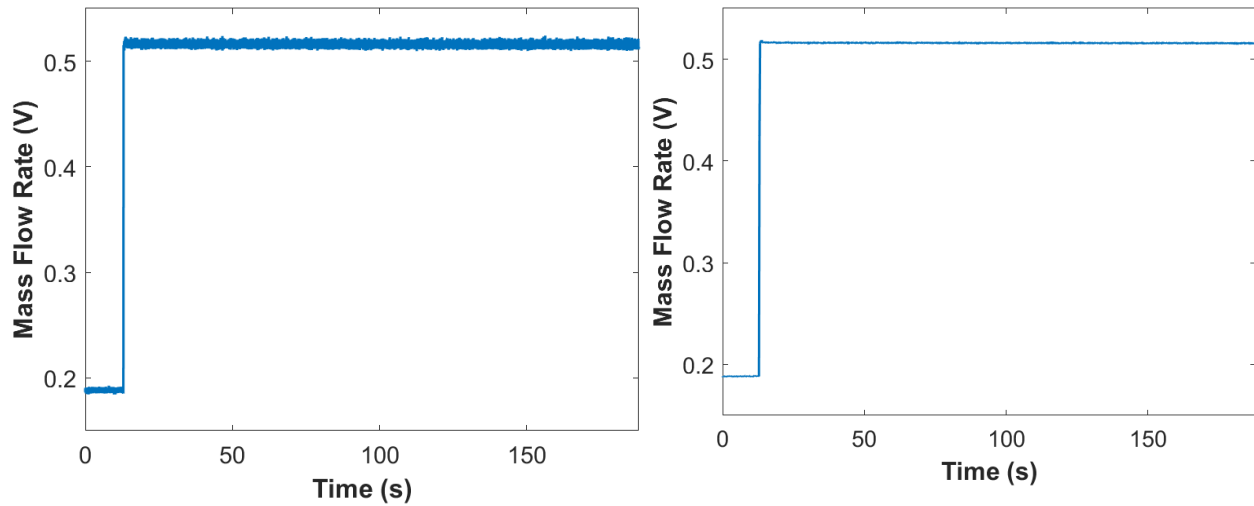


Figure 20-Unfiltered data (left) and filtered data (right)

The data for pressure, temperature, and mass flow rate were all filtered before analyzing. The test procedure is described more in depth in Appendix A. The 4 various experiments conducted are shown in Table 12. In these experiments, the mass flow rate, pressure box pressure, and pressure box temperature are recorded.

Table 12-List of experiments conducted

Test number	Description
1	No leakage scenario with the flow controller set to 0 Volts
2	Leakage with the flow controller set to 1 Volt
3	Leakage with the flow controller set to 2 Volts
4	Leakage with the flow controller set to 3 Volts

In addition to the pressure box data, the temperature and pressure outside the pressure box was recorded. The data obtained from this experimental setup will be discussed in section 4.3.

## 4.2 Thermal Model Updates for the Pressure Box

To validate the MCVT HIEM model, the pressure box is used to obtain experimental data for pressure leakage scenarios. The MCVT HIEM model was resized for the pressure box with a volume of 0.076 m<sup>3</sup>. A new thermal network was created based on the materials and dimensions used for pressure box structure as seen in Figure 21 and in Appendix B.

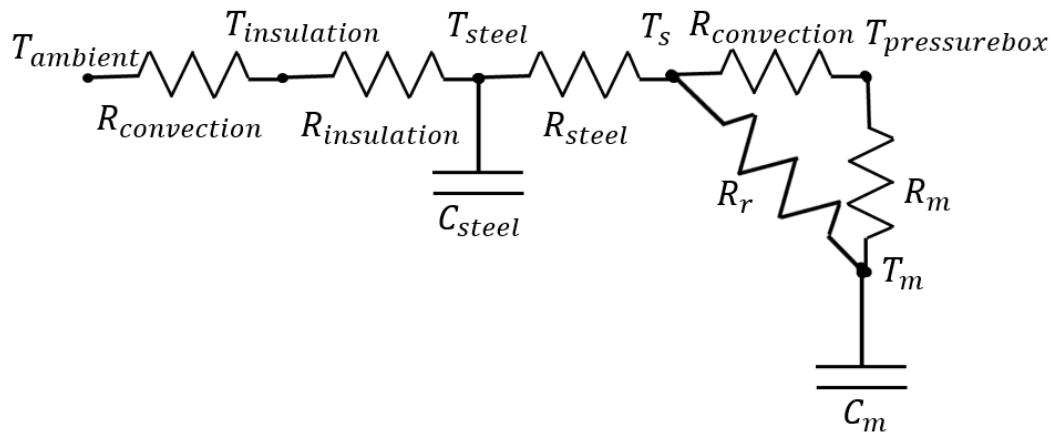


Figure 21-Thermal network for the pressure box

The resulting energy balance equations based on the thermal network in Figure 21 are:

$$\frac{T_s - T_{pressurebox}}{R_{convection}} + \frac{T_m - T_{pressurebox}}{R_m} = 0 \quad (Eqn. 35)$$

$$\frac{T_{steel} - T_s}{R_{steel}} + \frac{T_{pressurebox} - T_s}{R_{convection}} + \frac{T_m - T_s}{R_r} = 0 \quad (Eqn. 36)$$

$$\frac{T_{ambient} - T_{insulation}}{R_{convection}} + \frac{T_{steel} - T_{insulation}}{R_{insulation}} = 0 \quad (Eqn. 37)$$

The differential equations relating the temperature of each material as a function of time based on the thermal network in Figure 21 are shown below:

$$\frac{dT_{steel}}{dt} = \left( \frac{T_{insulation} - T_{steel}}{R_{insulation}C_{steel}} \right) + \left( \frac{T_s - T_{steel}}{R_{steel}C_{steel}} \right) \quad (Eqn. 38)$$

$$\frac{dT_m}{dt} = \left( \frac{T_{pressurebox} - T_m}{R_m C_m} \right) + \left( \frac{T_s - T_m}{R_r C_m} \right) \quad (Eqn. 39)$$

The values used for the resistances and capacitances are shown in Appendix C. After obtaining the

experimental data, it is then possible to compare with the computational results of the resized HIEM model. During this experimentation and comparison of results, the appropriate  $C_L$  and  $c_d$  values (Equations 24 and 26) as they apply to the pressure box can be determined. The loss coefficient “varies primarily with time, the opening geometry and the approaching wind direction due to the exterior pressure field” [18]. The discharge coefficient accounts for losses such as friction, heat, and noise. Both parameters are specific to individual systems and scenarios.

### 4.3 Methodology: Constant Mass Flow Rate

Initially, pressure leakages of the pressure box were done with a constant mass flow rate set by a mass flow controller. When the voltage signal is sent to the mass flow controller, the mass flow controller opens to allow a certain flow rate to leave the pressure box. The higher the voltage, the higher the mass flow rate. At each voltage, the area of the orifice is constantly changing as the pressure within the pressure box decreases in order to maintain a constant mass flow rate for the corresponding Volt. As previously mentioned, the pressure leakage calculation for MCVT requires a known area to determine the pressure in the interior environment. A fellow colleague in RETHi at Purdue has been researching how to calculate the area of an orifice based on mass flow rate and pressure. It was advised to use Equation 35 [34] to determine the area of the orifice based on the mass flow rate and changing pressure values.

$$\dot{m}_e = \frac{\rho_{01}}{p_{01}^{1/\gamma}} \left( \frac{2}{\gamma + 1} \right)^{\frac{1}{\gamma-1}} A_e \sqrt{\frac{2\gamma p_{01}^{1/\gamma}}{(\gamma + 1)\rho_{01}}} p_0^{\frac{\gamma+1}{2\gamma}} \quad (Eqn. 40)$$

In Equation 35,  $\dot{m}_e$  is the mass flow rate exiting ( $kg/s$ ),  $\rho_{01}$  is the initial density ( $kg/m^3$ ),  $\gamma$  is the ratio of the specific heat of air,  $p_{01}$  is the initial pressure of the pressure box (the pressure of the pressure box at the beginning of the experiment, (Pa)),  $p_0$  is the interior pressure of the pressure box (Pa), and  $A_e$  is the effective area of the orifice ( $m^2$ ). However,  $A_e$  is the product of the geometric area of the orifice and the discharge coefficient (Equation 41), not strictly the geometric area.

$$A_e = c_d \cdot A_g \quad (Eqn. 41)$$

The discharge coefficient is used in fluid dynamics. It is the ratio of the actual discharge to the ideal discharge [35]. It accounts for friction, the thickness of the boundary layer, and assumes that the properties measured downstream of the orifice exit represent the conditions at the exit [35].

This method was executed regardless to observe any possible correlation and trends between the experimental pressure data and modeled pressure data. The effective area in Equation 41 is also used in Equation 26. The calculated effective area is used as an input into the Simulink model. For this reason,  $c_d$  was set to 1 in Equation 26 in the model. However, Equation 24 requires a geometric area, not an effective area. It was not possible to obtain the  $c_d$  value using the variable area flow meter. This causes the geometric area to remain unknown. The effective area was used as the geometric area in Equation 26 for modeling purposes. The effective area obtained from Equation 40 is then used to validate the methodology for modeling pressure leakages. The effective area of the leakage, external pressure, and other known parameters as discussed in Chapter 3 are used to model the pressure of the interior environment of the pressure box.

### 4.3.1 Pressure Box Data Collected

This section discusses experimental data of the pressure box for 0, 1, 2, and 3 Volts along with the calculated effective area using Equation 40. For a flow controller with 0 Volts, there is no leakage occurring. However, there is still a pressure loss over time—indicating an unintentional leak in the pressure box. Figure 22 shows the temperature and pressure of the pressure box for 0 Volts.

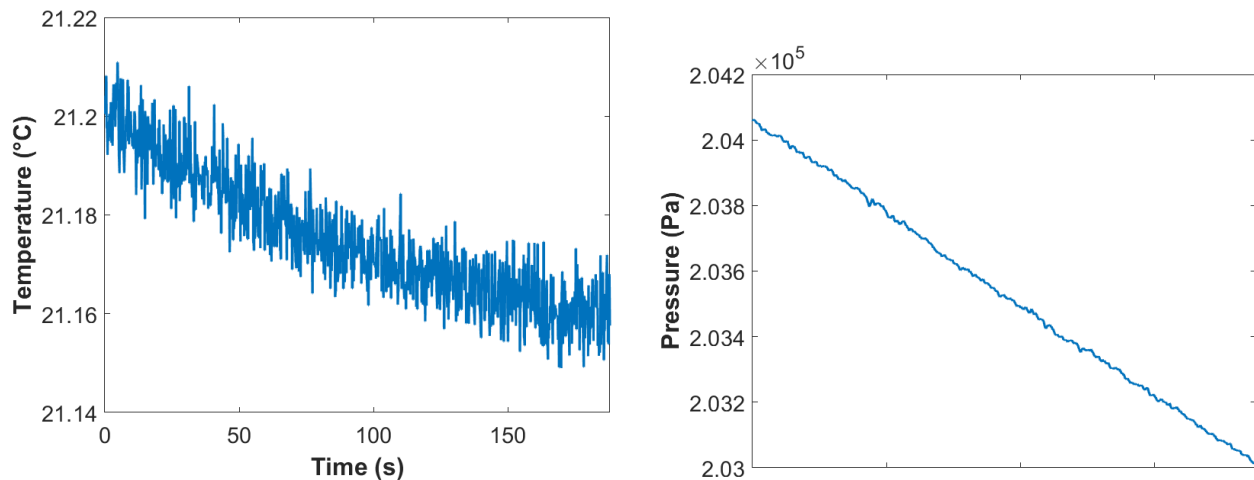


Figure 22-Temperature (left) and pressure (right) for the pressure box at 0 Volts

Over a duration of 200 seconds, it is observed that the pressure decreases approximately 0.59% for this specific 0 Volt scenario. This leads to a slight decrease in temperature as well. In order to model this pressure drop, the mass flow rate was measured to calculate the effective area of leakage

using Equation 40. Figure 23 shows the recorded mass flow rate and calculated effective area for a mass flow controller at 0 Volts.

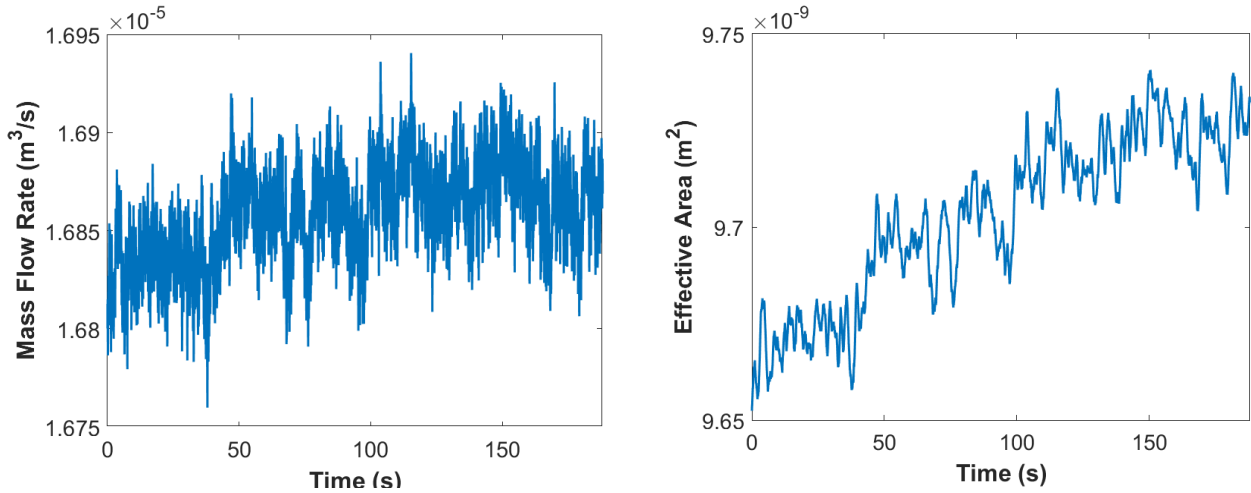


Figure 23-Mass flow rate (left) and effective area (right) of pressure box for 0 Volts

When the mass flow controller is set to 1 Volt, a very small, variable area is used to keep the mass flow at a minimal rate. Figure 24 shows the filtered, experimental data of temperature, pressure, and mass flow rate for 1 Volt. The calculated effective area using Equation 40 for the pressure box leakage using 1 Volt is also shown in Figure 24.

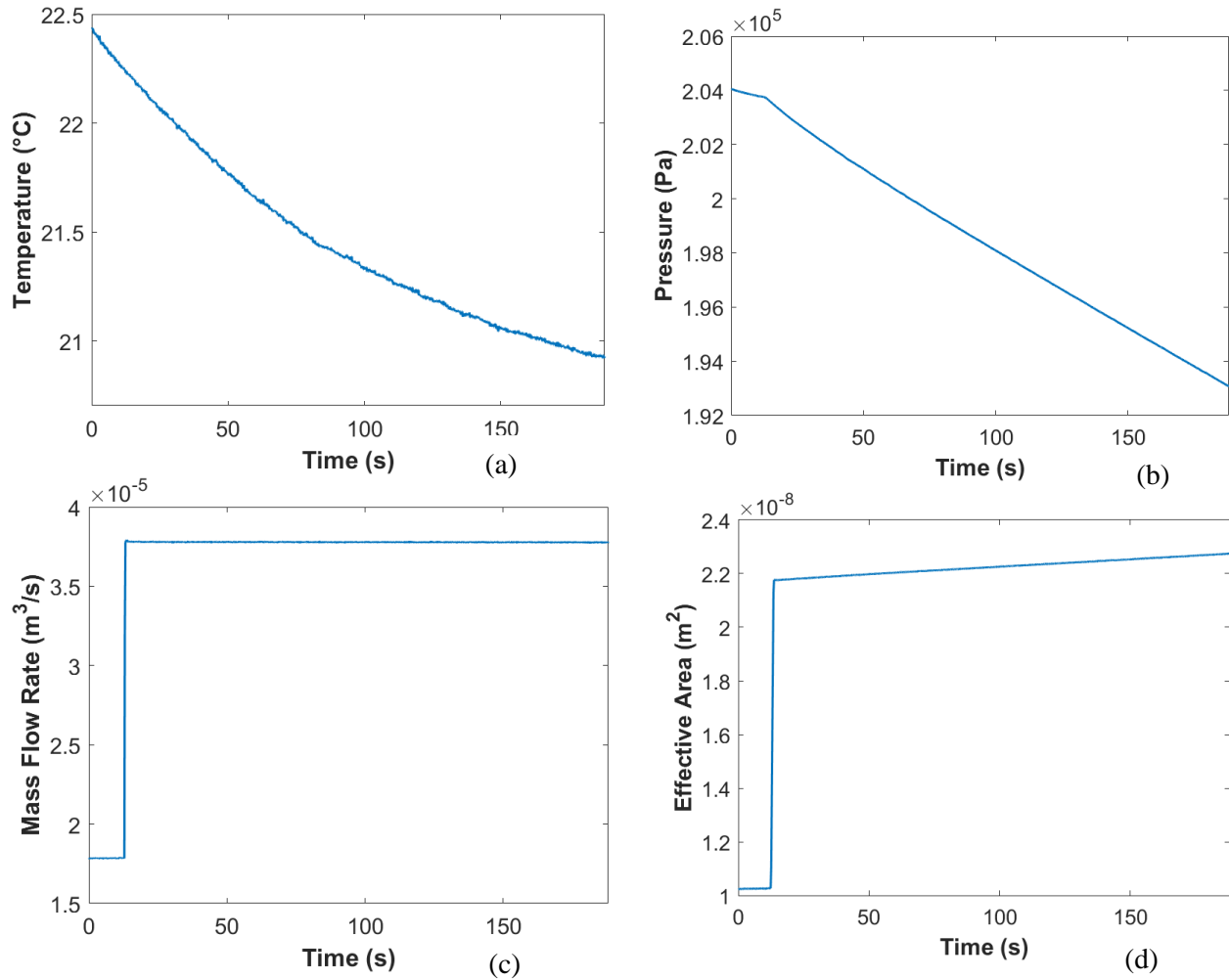


Figure 24-Temperature (a), pressure (b), mass flow rate (c), and effective area (d) of the pressure box at 1 Volt

In Figure 24, it can be seen that when the 1-Volt leakage is initiated, the pressure begins to drop. There is still a decrease in temperature and pressure before the voltage is initiated. This can most likely be contributed to the unintentional leak of the pressure box. The decrease in pressure causes a direct effect on temperature as well. The mass flow rate recorded was nearly  $3.7 \times 10^{-5} \text{ m}^3/\text{s}$ . It is observed that the effective area slightly increases with the constant mass flow rate due to the decreasing pressure within the pressure box. This makes sense since the pressure box pressure is consistently declining, and the area regularly adjusts to maintain a constant mass flow rate.

When the flow controller is set to 2 Volts, the mass flow rate is intended to be larger than the 1-Volt setting. The larger mass flow rate leads to a larger area of leakage to allow a larger amount of air mass to leave the pressure box. Figure 25 shows the filtered, experimental temperature, pressure, and mass flow rate for 2 Volts. Figure 25 also has the calculated effective area of the pressure box when the mass flow controller is set to 2 Volts.

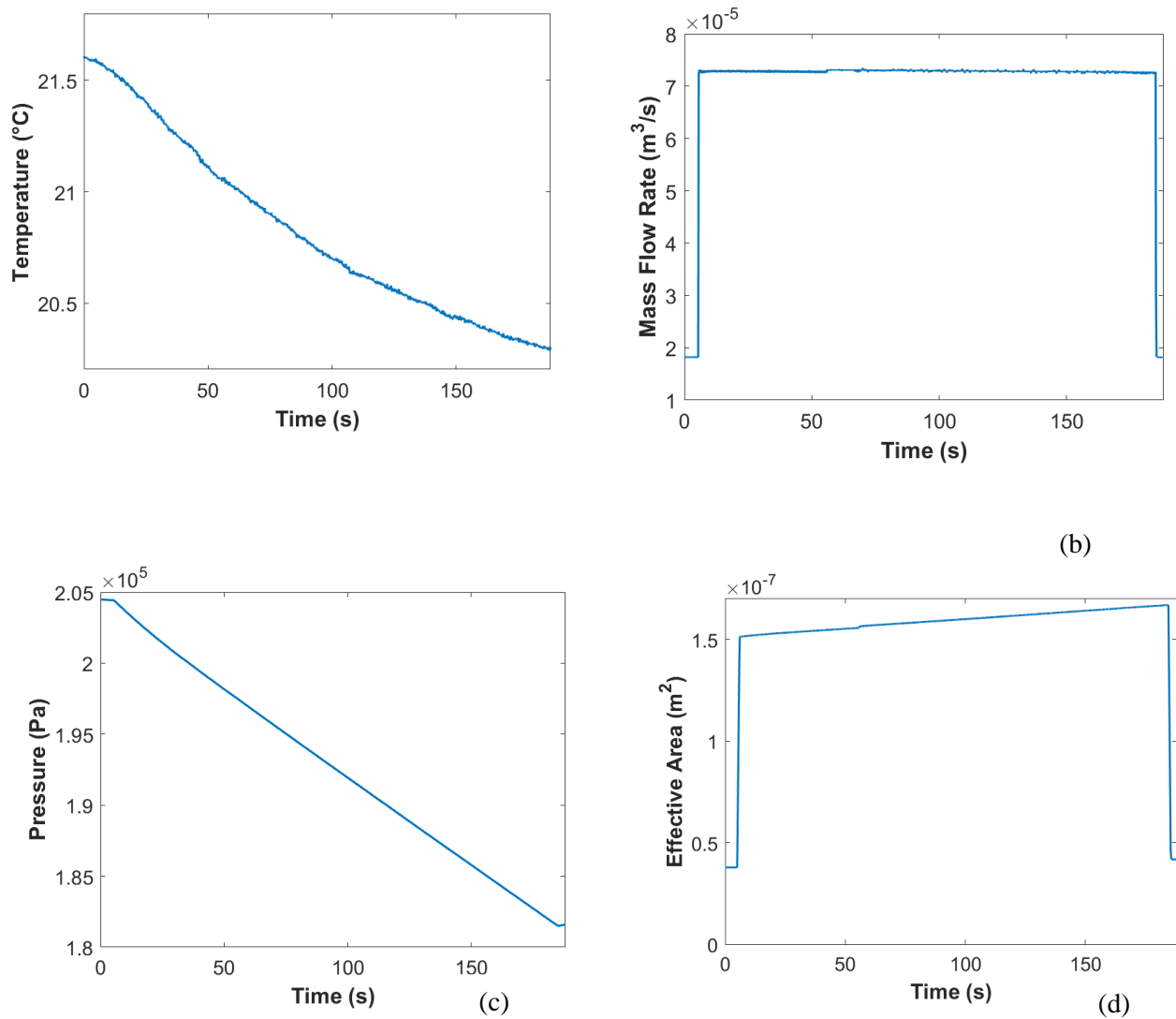


Figure 25-Temperature (a), pressure (b), mass flow rate (c), and effective area (d) of the pressure box at 2 Volts

It is observed that with the larger area of leakage, there is also a larger mass flow rate. This larger mass flow leaving the pressure box leads to a steeper decrease in pressure than in the 1 Volt scenario. Therefore, a corresponding decrease in temperature is steeper than the 1 Volt case.

When the mass flow controller is set to 3 Volts, there is a larger mass flow rate leaving the system than for 2 Volts. Figure 26 displays the filtered results for when the mass flow controller is set to 3 Volts along with the calculated effective area.

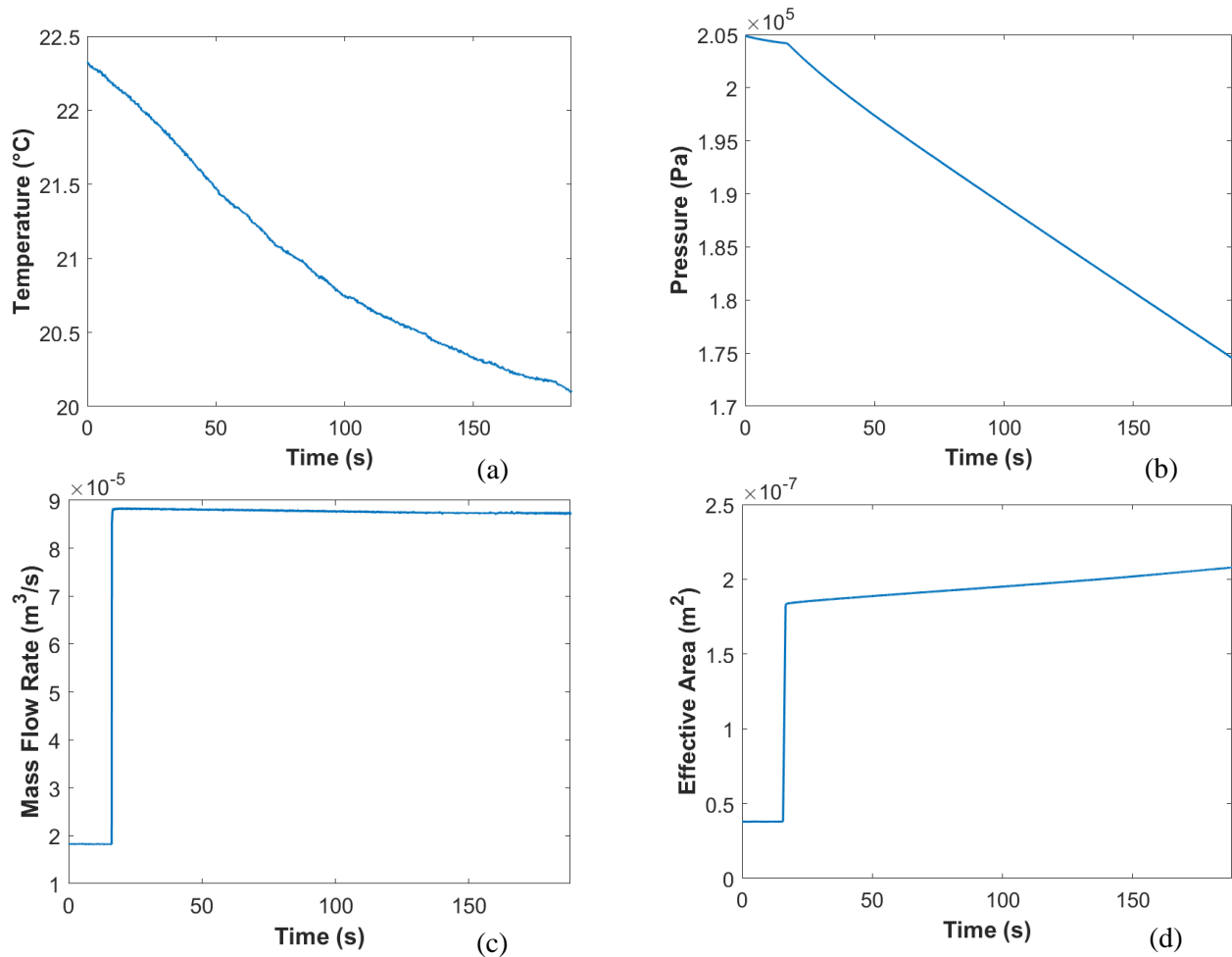


Figure 26-Temperature (a), pressure (b), mass flow rate (c), and effective area (d) of the pressure box at 3 Volts

The larger mass flow rate contributes to a larger area of leakage than for the 2 Volt case. As the pressure within the pressure box decreases, the leakage area increases to maintain a constant mass flow rate. Since pressure and temperature are coupled, the temperature also decreases.

### 4.3.2 Pressure Box Model Results

Using the effective area calculated from the results of the data collected, it is possible to model the leakage scenarios in the CPT model based on the methodology used for MCVT. The effective area is used as an input in the Simulink pressure box model. Since the area used is the effective area, the  $c_d$  value used in Equation 26 was set to 1 as explained in the previous section. The only remaining parameter to parameterize is the loss coefficient from Equation 24. After running numerous scenarios with a variety of  $C_L$  values, it was determined that a constant  $C_L$  of 5 provided the best results. Figure 27 shows the temperature and pressure for the pressure box when a 0-Volt case is simulated using the modeling methodology described earlier.

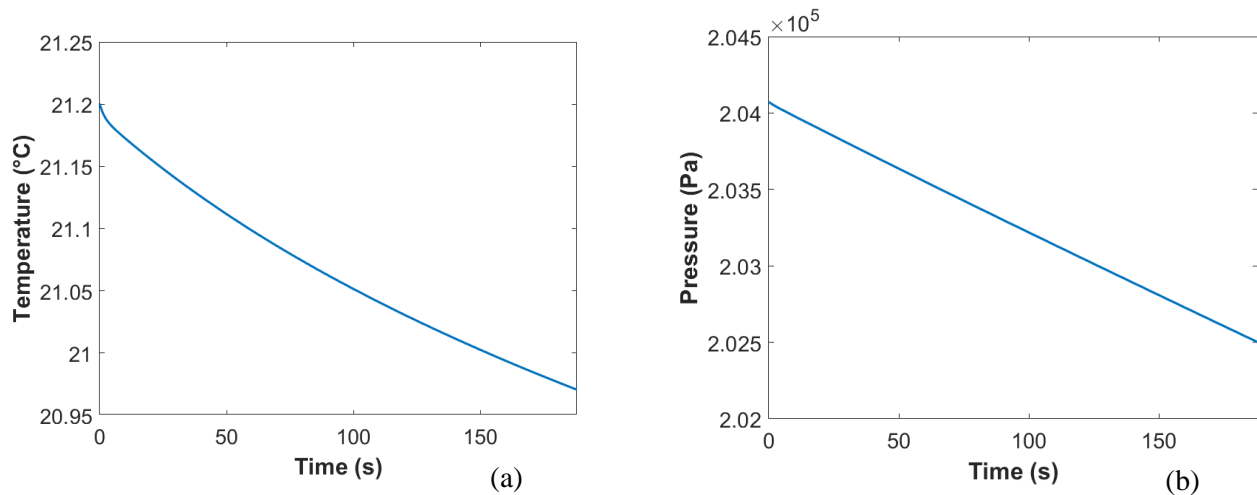


Figure 27-Temperature (a) and pressure (b) for 0-Volt pressure box model

In Figure 27, it is observed that using the determined effective area for a 0-Volt case causes a very small decrease in both temperature and pressure for the pressure box model. Once more, a 0-Volt scenario is supposed to have no leakage. To accurately model the pressure box, the calculated effective area for the 0-Volt scenario was used to attempt to model the unidentified leak. Figure 28 shows the data comparison of temperature and pressure between the experimental data and the model results. The red band on the temperature graph depicts the  $\pm 0.5^\circ\text{C}$  uncertainty error of the thermocouple. This uncertainty range is provided by the manufacturer of the thermocouple as the range in which the temperature readings may contain an error. The red band on the pressure graph shows  $\pm 0.2\%$  full scale uncertainty error of the pressure sensors. This is similar to the  $\pm 0.5^\circ\text{C}$  uncertainty for temperature. The manufacturer of the pressure sensors reports a  $\pm 0.2\%$  uncertainty in pressure readings. The purple band shows a  $\pm 5.0\%$  experimental error on the pressure graph.

This experimental error is used to help validate the model's accuracy. There is not a corresponding experimental error percentage on the temperature graph. This is because temperature is never compared using percentages. It was decided to attempt to remain within the  $\pm 0.5^\circ\text{C}$  uncertainty for temperature.

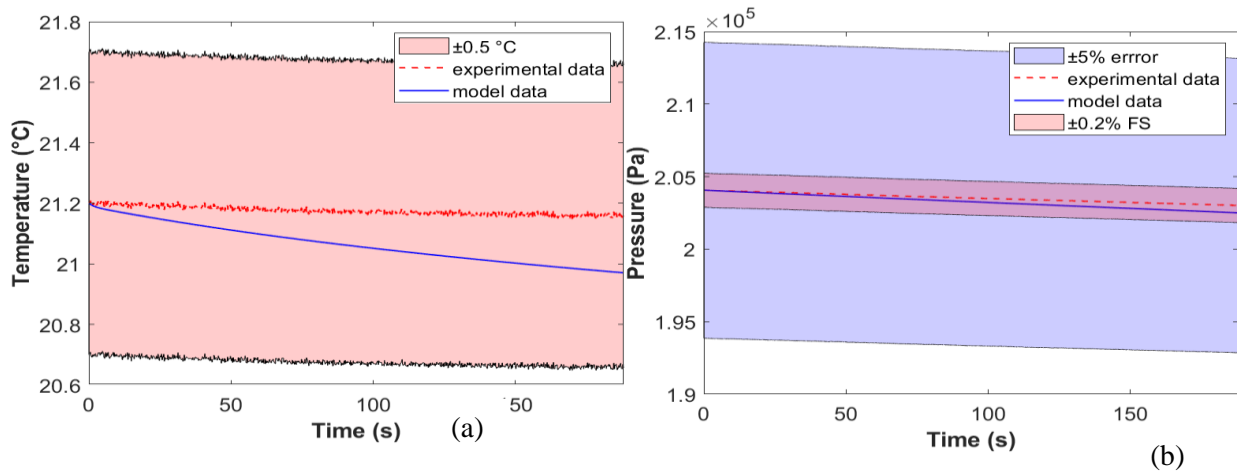


Figure 28-Data comparison of temperature (a) and pressure (b) for 0-Volts

Figure 29 displays the temperature and pressure for a 1-Volt leakage simulation using the calculated effective area as an input to the Simulink model from Figure 22.

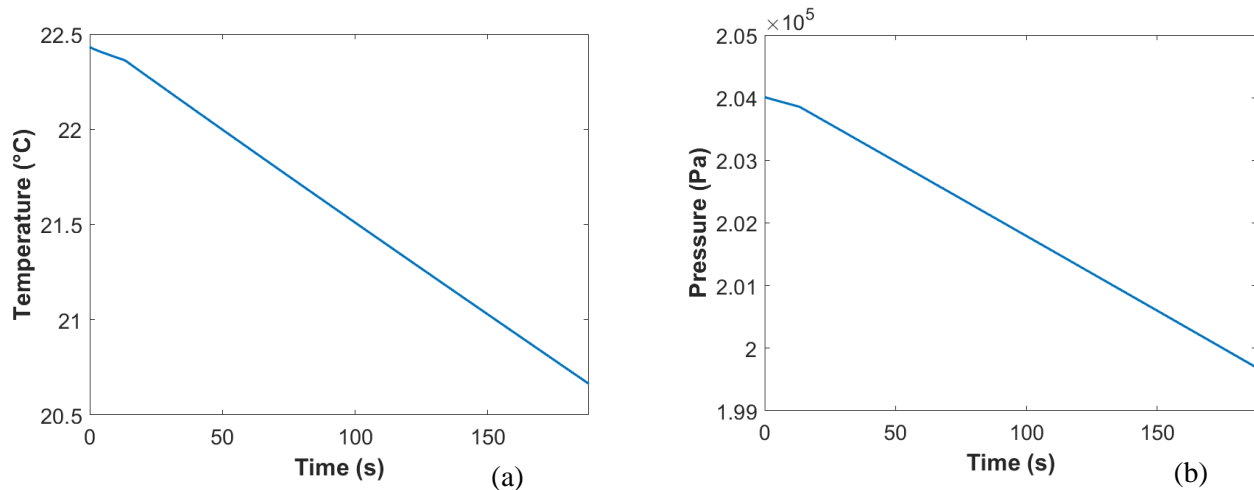


Figure 29-Temperature (a) and pressure (b) for 1-Volt pressure box model

Figure 29 reveals that with a larger effective area, there is a larger temperature and pressure drop

within the same time-period. It is observed that before the Volt is initiated, there is still a temperature and pressure drop. This behavior is mostly occurring due to the unknown leakage in the pressure box. Figure 30 shows the data comparison for this 1-Volt scenario.

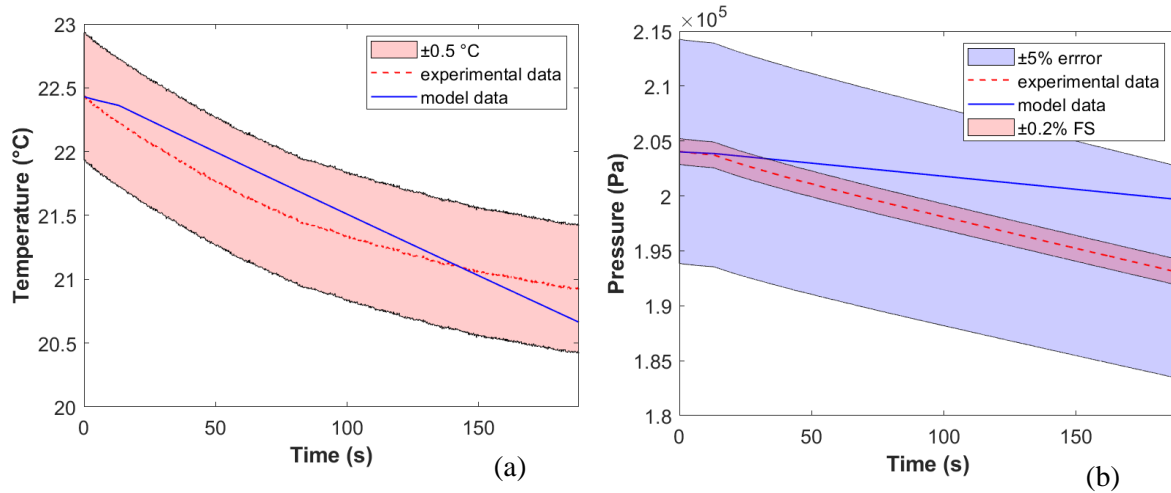


Figure 30-Data of temperature (a) and pressure (b) comparison for 1-Volt

In Figure 30, it is observed that the thermal behavior of the model is not precisely following the experimental. Figure 31 demonstrates the temperature and pressure for a 2-Volt leakage simulation.

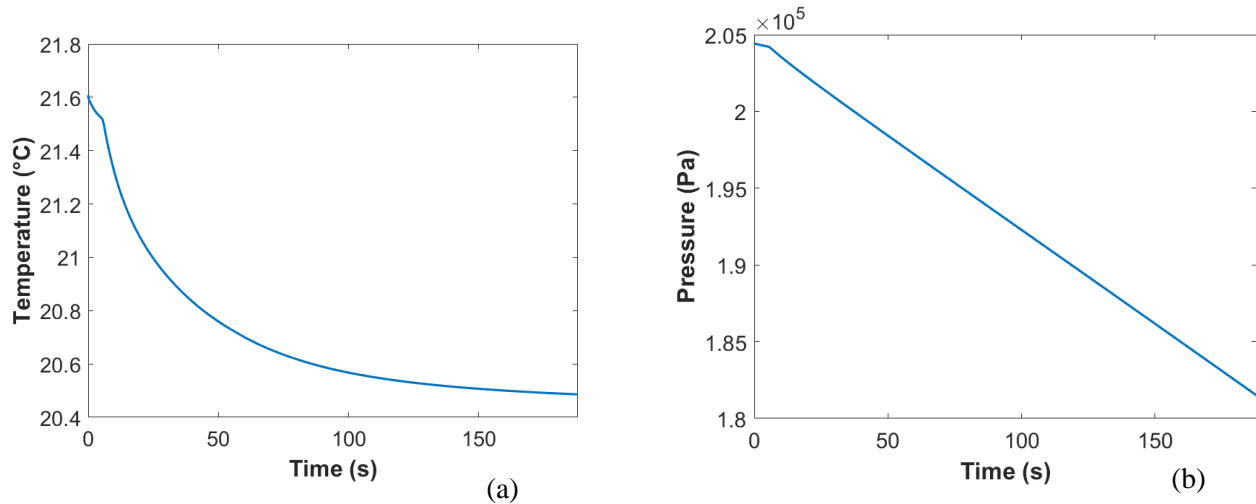


Figure 31-Temperature (a) and pressure (b) for 2-Volt pressure box model

It is yet again observed that there is a temperature and pressure decrease before the Volt is initiated. Once the Volt is initiated, the decrease in temperature and pressure is larger than the 1-Volt case aforementioned. Figure 31 shows the data comparison for a 2-Volts scenario using the calculated effective area from Figure 25 as an input to the Simulink pressure box model.

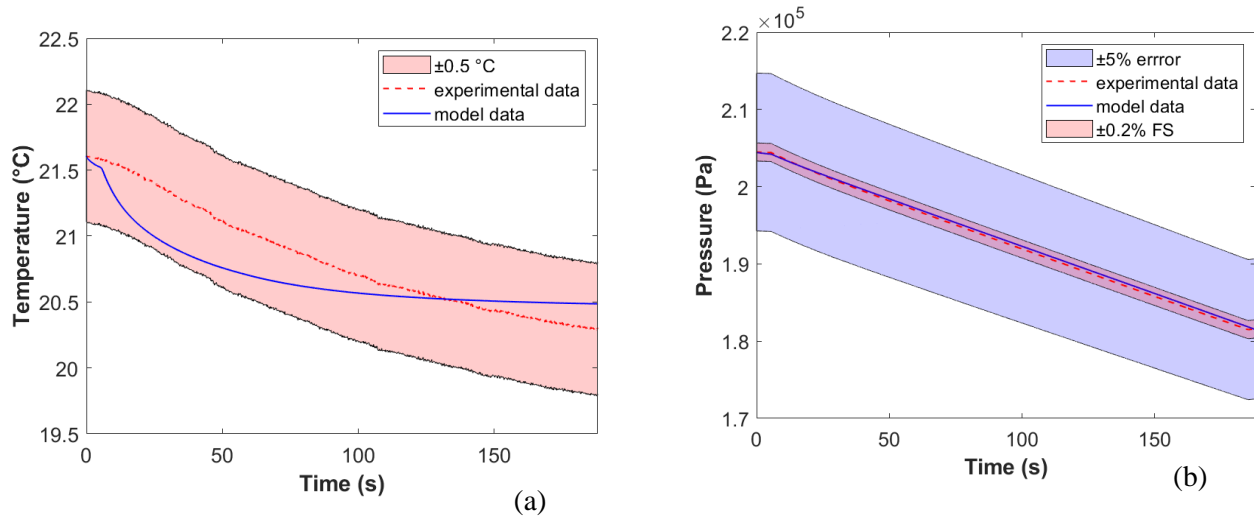


Figure 32-Data comparison of temperature (a) and pressure (b) for 2-Volts

The results seen in Figure 32 show that the model is still within an acceptable range; however, the behavior of the temperature model is not entirely similar to that of recorded temperature. The model appears to have a piece-wise behavior that cannot be physically explained. This can most likely be contributed to the values used for the thermal capacitances and resistances. These exact values would need to be obtained through further testing rather than the use of theoretical values. By doing so, it may be possible to capture the thermal behavior of the pressure box more precisely.

Figure 33 demonstrates the temperature and pressure for a 3-Volt leakage simulation using the calculated effective area from Figure 26.

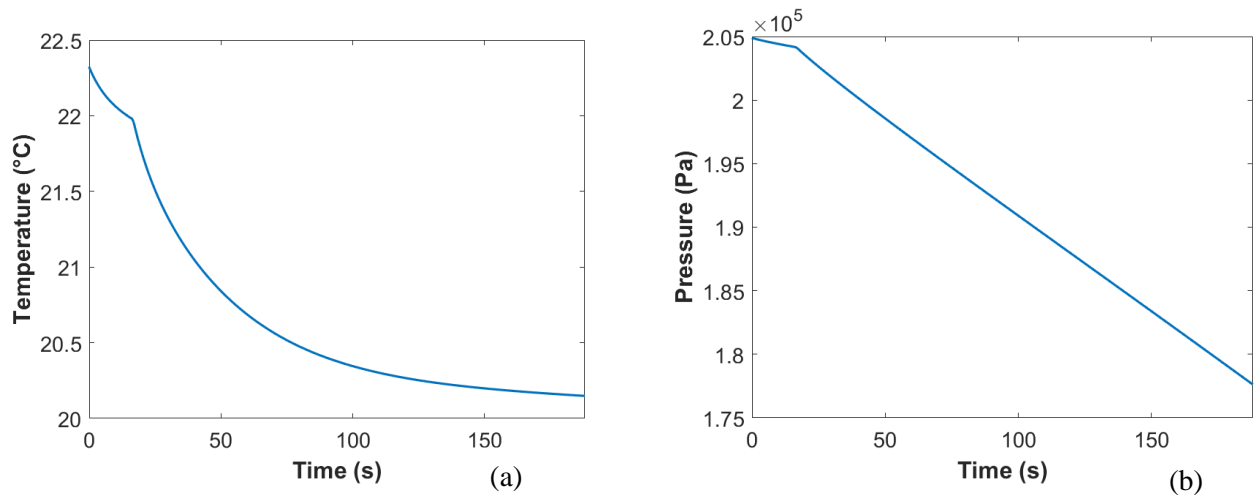


Figure 33-Temperature (a) and pressure (b) for 3-Volt pressure box model

The pattern persists in the model—the larger the effective area, the larger the temperature and pressure drop within the time-period. Figure 34 shows the comparison for the model results and the test data.

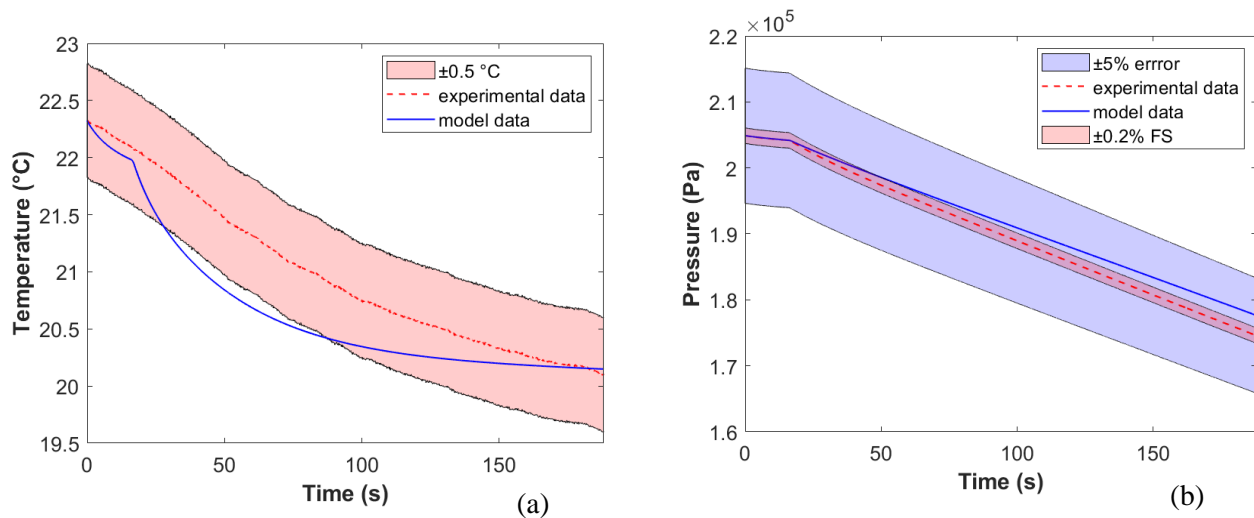


Figure 34-Data comparison of temperature (a) and pressure (b) for 3-Volts

It can be seen here that the temperature model is mostly within an acceptable range, yet the still has a behavior inconsistent with the experimental temperature. Once more, this can be contributed to values that would need to be experimentally obtained in an attempt to capture a more accurate behavior. Further testing would be needed to validate this hypothesis.

In order to better model the pressure of the pressure box, a leakage test with a known area of leakage, rather than a calculated effective area, would be ideal. Using this test setup with a known area of leakage, Equation 26 can be used to calculate an appropriate  $c_d$  value. Then,  $C_L$  from Equation 24 would be the only variable that would need parameterization. Furthermore, for the temperature data collected, the thermocouples may not have been securely attached within the pressure box. This would cause a slight inaccuracy in the temperature data collected during the experiment. Overall, the model used to determine the temperature and pressure of the pressure box is within accuracy. The temperature model is mostly within the  $\pm 0.5^\circ\text{C}$  uncertainty and the pressure model is within  $\pm 5\%$  error. This methodology can subsequently be used to determine the temperature and pressure of HIEM used in MCVT to model the interior environment of lunar habitats.

## 5. MCVT RESULTS

This section details the results of HIEM within MCVT (as discussed in Sections 3.2-3.4) for normal conditions and various disturbance scenarios (Section 3.1.1). These simulations are used to predict the interior environment behavior when different disturbances occur. The pressure and temperature of the interior environment and airlock are seen in Figures 35 and 36. Figure 37 shows the thermal load provided by ECLSS. ECLSS can only support either the interior environment or the airlock when the inner door is closed. When no disturbances are present, the inner door is open. When a disturbance occurs, the inner door closes. Essentially, ECLSS only has the ability to manage the temperature and pressure of one zone at a time when the inner door is closed. Since the inner door between the interior environment and the airlock is closed as a safety precaution under different disturbances, ECLSS supports the undamaged or healthy zone. As a result, the ECLSS thermal load seen in Figure 37 is the same for all scenarios except an airlock failure with an intensity level of 3.

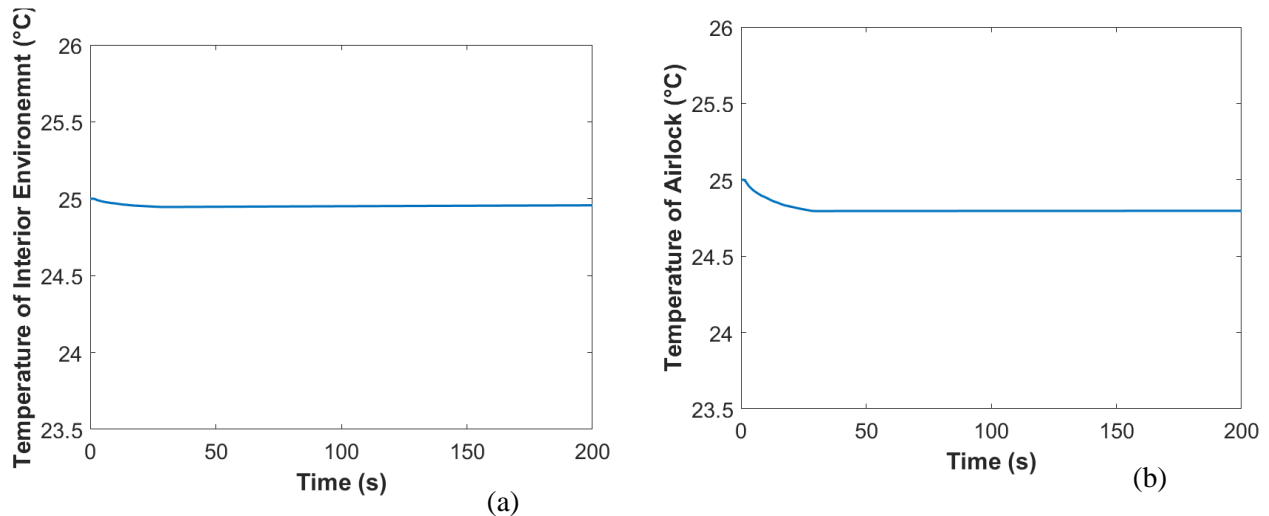


Figure 35-Temperature of HIEM (a) and the airlock (b) under normal conditions

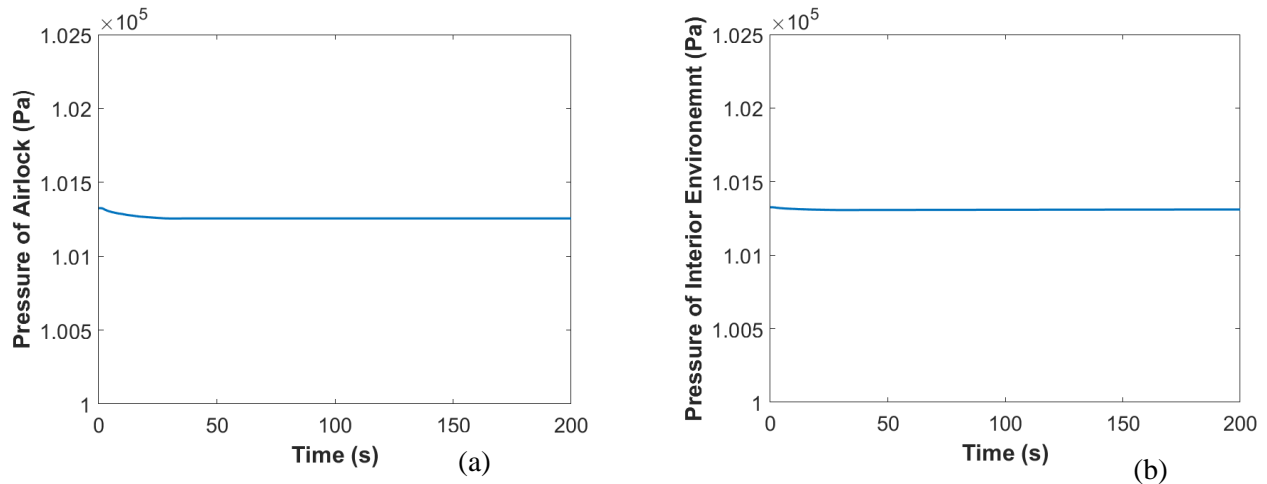


Figure 36. Pressure of HIEM (a) and the airlock (b) under normal conditions

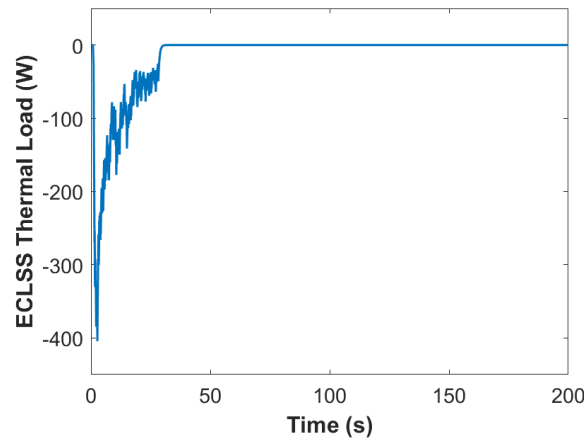


Figure 37-ECLSS thermal load distributed to HIEM and the airlock under normal conditions

There are very slight temperature and pressure differences between the interior environment and the airlock. This can most likely be contributed to the fact that the structural subsystem provides the temperature of the inner wall of the structure which is used to calculate the heat release rate for the interior environment. Meanwhile, the airlock thermal network was created to calculate the temperature of the inner wall of the airlock structure as discussed in Section 3.2.2. This inconsistency is due to the fact that the actual airlock is not yet a part of the MCVT code. The airlock model will be incorporated in the next version of MCVT. Figure 36 shows that ECLSS is providing a thermal load to the interior environment in the first few seconds of the simulation. Since the interior environment and airlock's temperature and pressure are both within a comfortable range, this thermal load is most likely caused by the set initial conditions of MCVT.

Correspondingly, the initial minor decrease in temperature and pressure of the two zones from Figures 35 and 36 reflects the ECLSS thermal load delivery from Figure 36 that is included in the temperature and pressure calculation at each time step.

When there is a fire disturbance with an intensity level of 2, the fire radius is a constant 0.05 cm as discussed in Table 4 and seen in Figure 38. Once the fire disturbance is initiated in the interior environment, the inner door separating the interior environment and the airlock is closed, and ECLSS only provides support to the airlock.

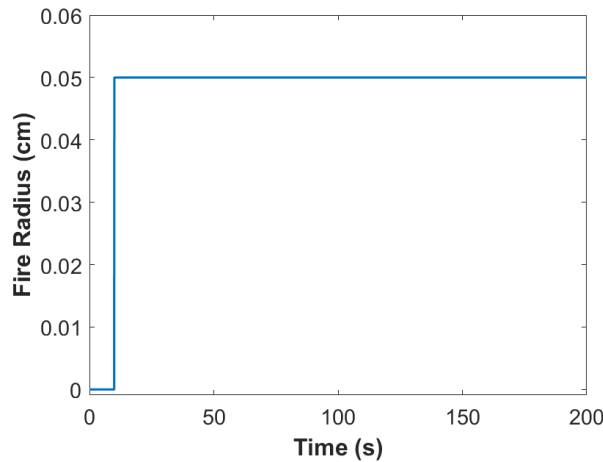


Figure 38-Fire radius for fire intensity level 2

Figures 39 and 40 show the temperature and pressure increase in the interior environment due to the fire with a constant radius.

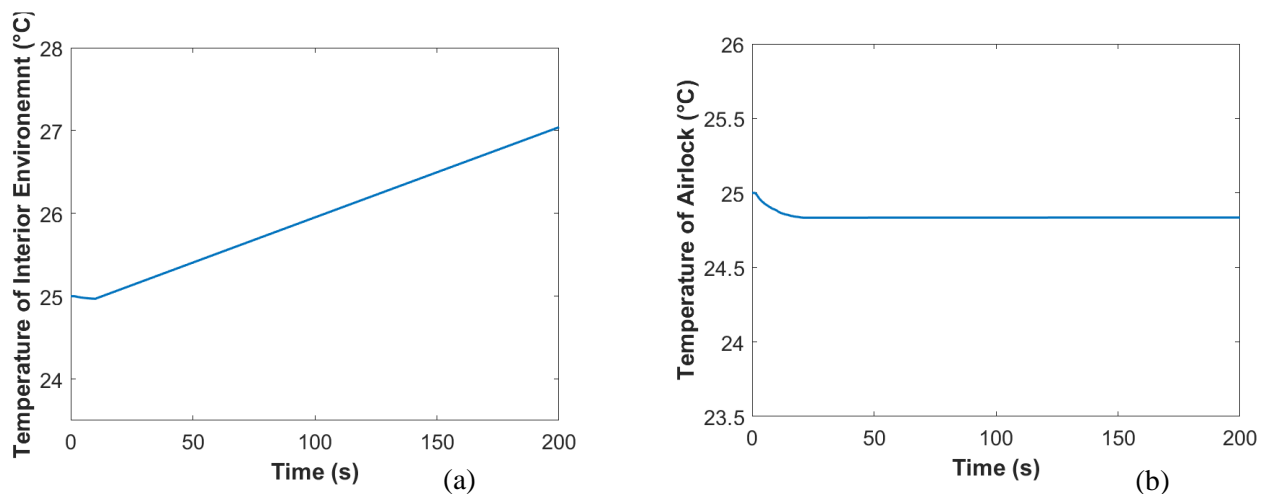


Figure 39. Temperature of HIEM (a) and the airlock (b) for fire intensity level 2

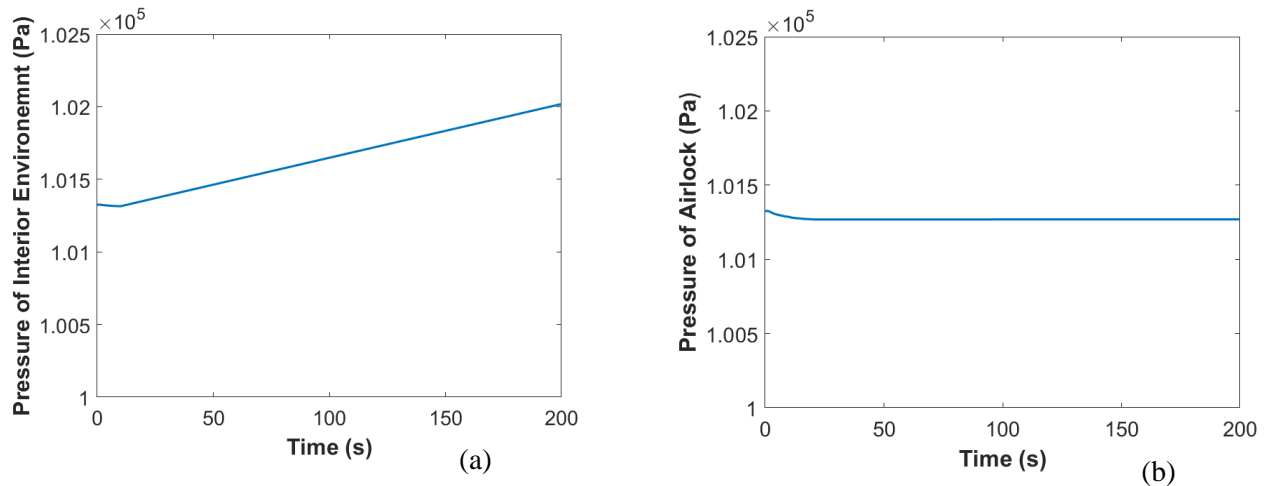


Figure 40. Pressure of the HIEM (a) and the airlock (b) for fire intensity level 2

The fire is set in the interior environment thereby causing the interior environment's temperature and pressure increase. The airlock's closed inner door protects the airlock chamber from the fire disturbance.

Figure 41 shows the slow increase in fire radius when there is a fire with an intensity level of 3.

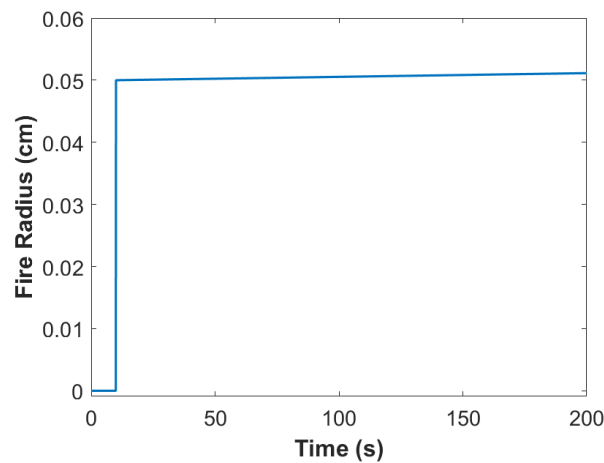


Figure 41. Fire radius for fire intensity level 3

The fire radius is initially 0.05cm, but steadily increases at a rate of 0.015cm/sec.

Figures 42 and 43 show the temperature and pressure of the interior environment and airlock for a fire intensity level of 3.

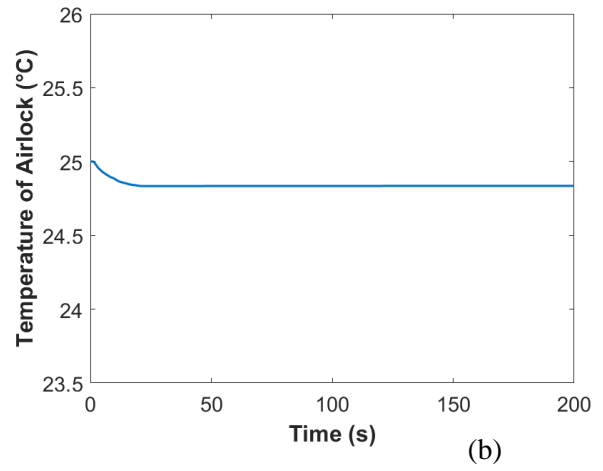
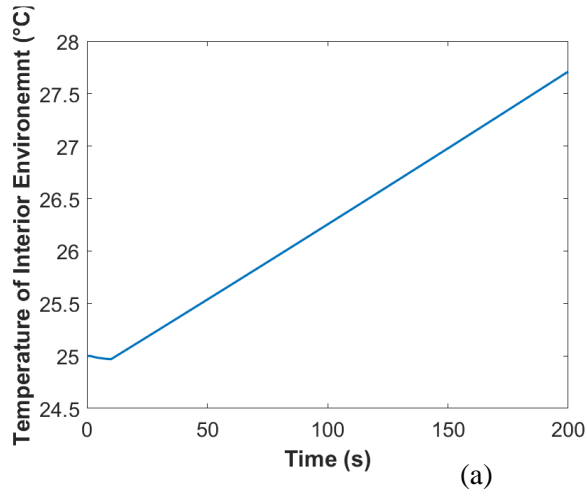


Figure 42-Temperature of HIEM (a) and the airlock (b) for fire intensity level 3

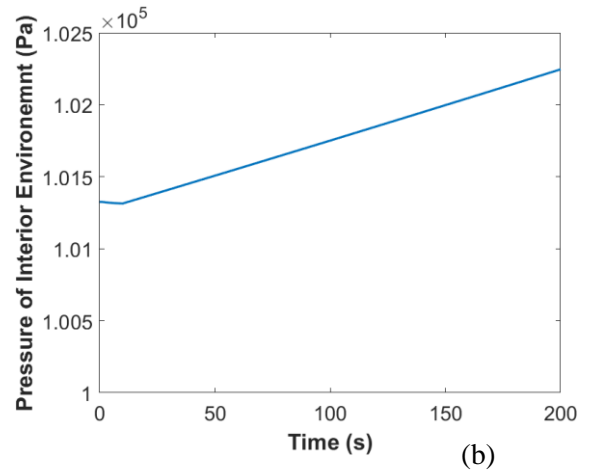
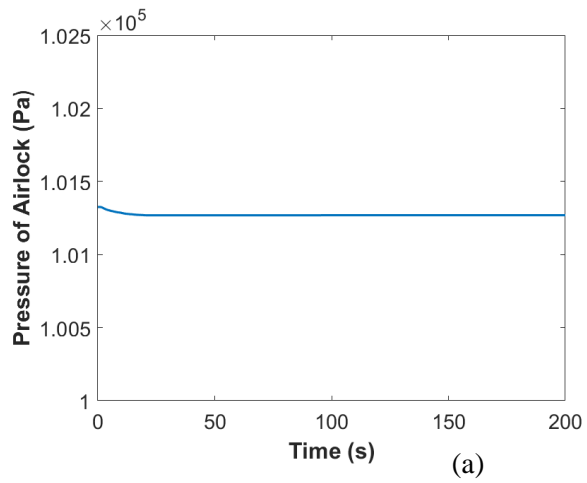


Figure 43- Pressure of the HIEM (a) and the airlock (b) for fire intensity level 3

Figure 44 shows the fire radius for a fire intensity level of 4.

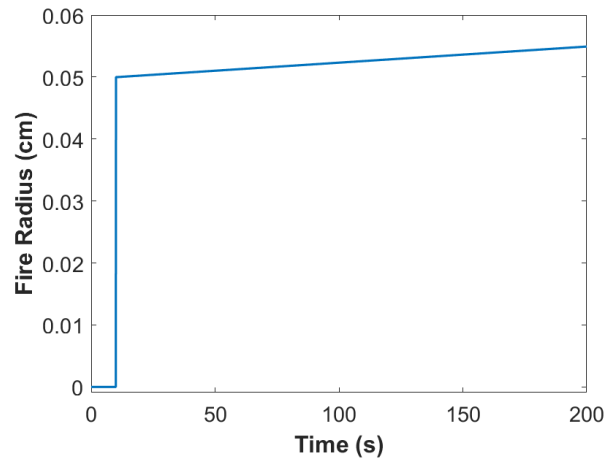


Figure 44. Fire radius for fire intensity level 4

The fire radius for intensity level 4 starts at 0.05cm and increases 0.067cm/sec.

Figures 45 and 46 show the temperature and pressure for the interior environment and airlock for a fire intensity level 4.

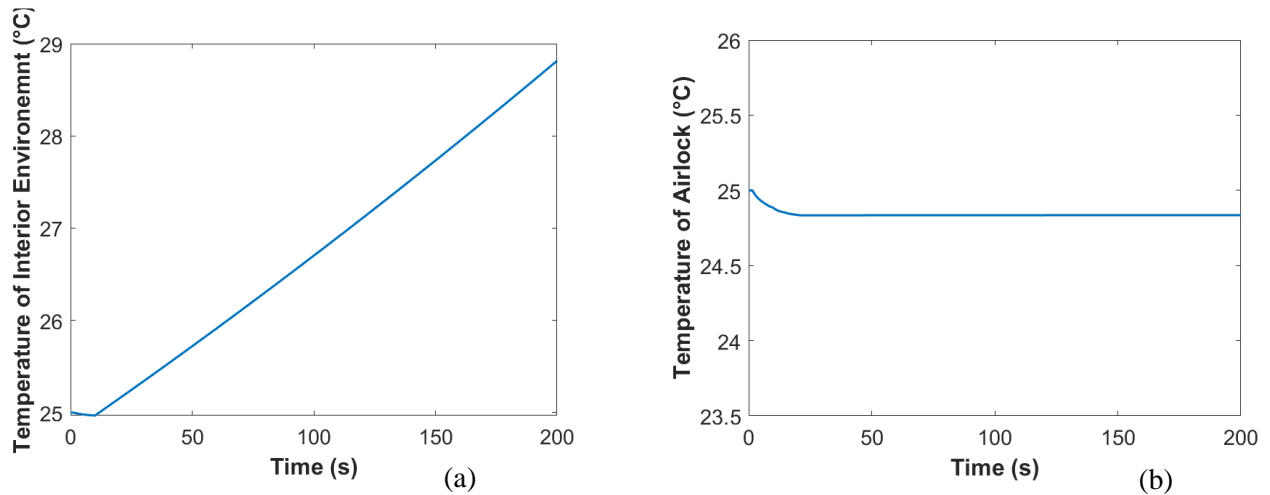


Figure 45. Temperature of HIEM (a) and the airlock (b) for fire intensity level 4

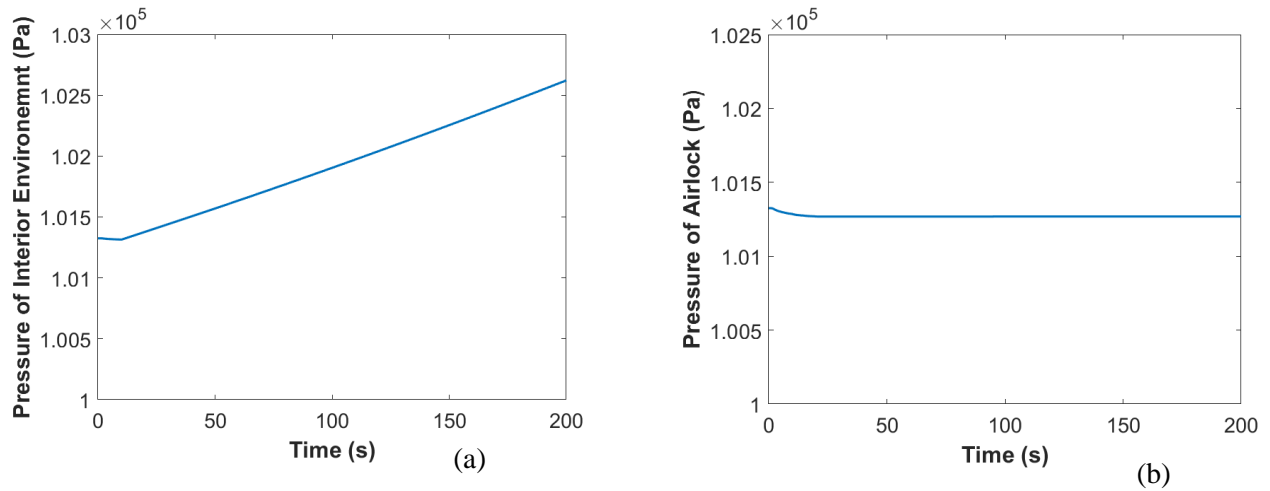


Figure 46. Pressure of HIEM (a) and the airlock (b) for fire intensity level 4

It is evident that compared to a fire intensity level 3, that the larger increase in fire radius in intensity level 4 contributes to a larger temperature and pressure increase in the interior environment.

The radius for fire intensity level 5 is shown below in Figure 47.

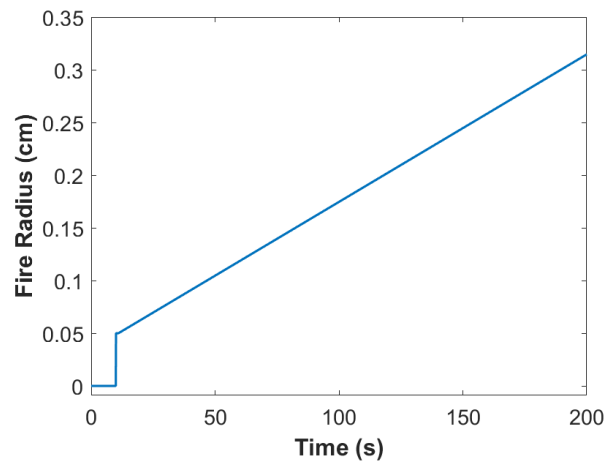


Figure 47. Fire radius for fire intensity level 5

For fire intensity level 5, the fire radius is initially 0.05cm and increases 3.5cm/s.

The temperature and pressure for fire intensity level 5 are shown in Figures 47 and 48.

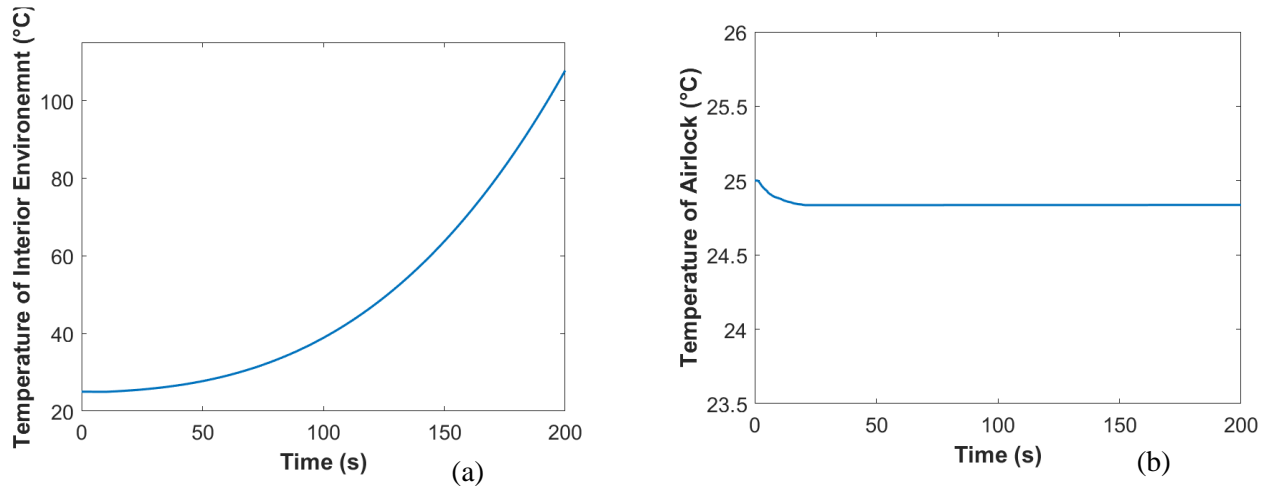


Figure 48- Temperature of HIEM (a) and the airlock (b) for fire intensity level 5

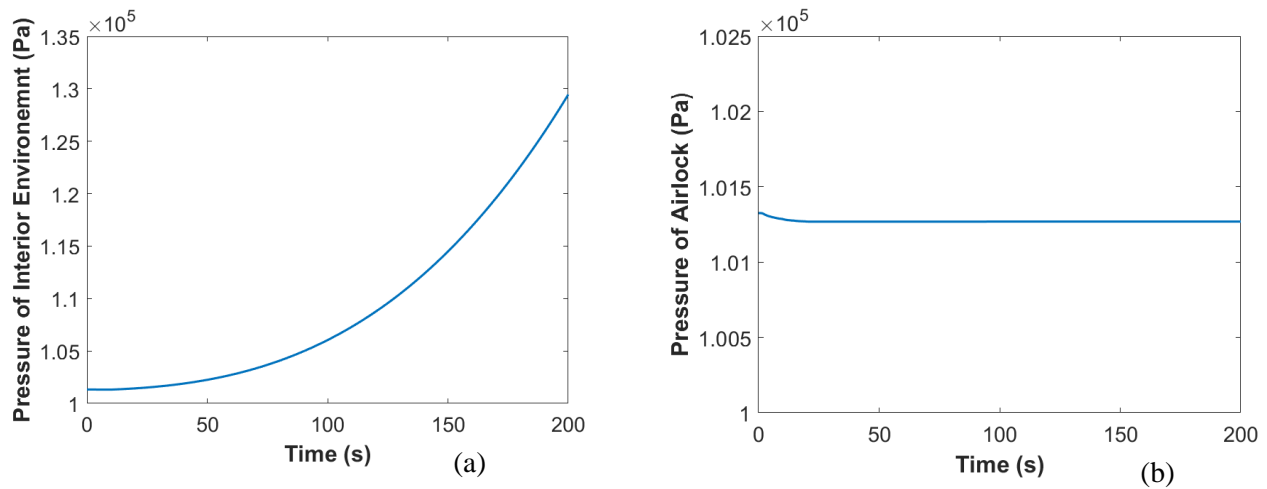


Figure 49. Pressure of HIEM (a) and the airlock (b) for fire intensity level 5

Figures 48 and 49 show that this increasing fire causes a large increase in temperature and pressure when compared to the other fire intensity levels.

When there is a meteorite impact with an intensity level of 4, there is a hole radius of 0.005m in the interior environment structure. Figures 50 and 51 show the temperature and pressure of the interior environment and the airlock.

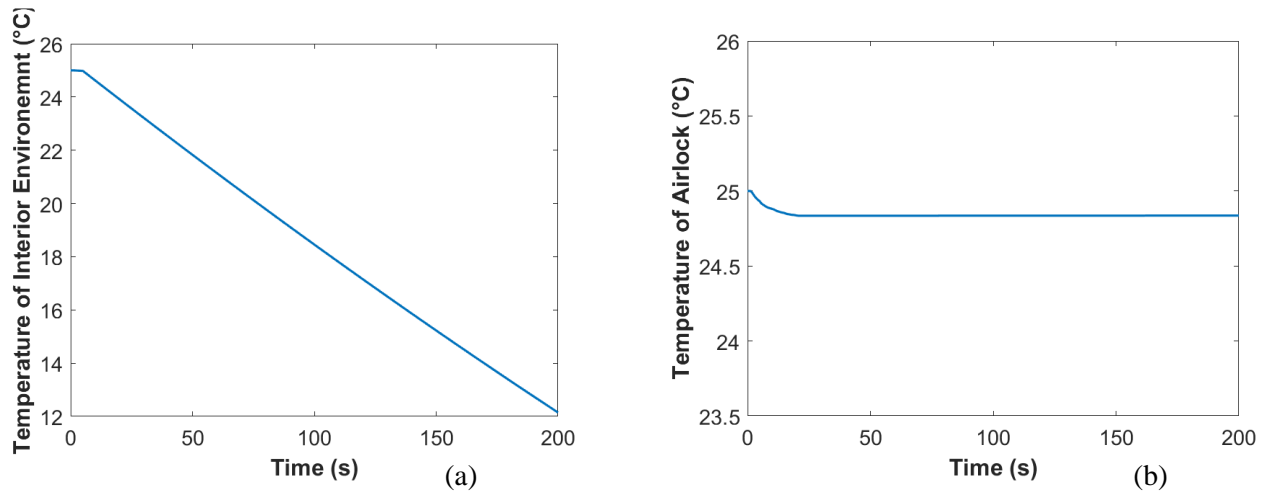


Figure 50. Temperature of HIEM (a) and the airlock (b) for meteorite intensity level 4

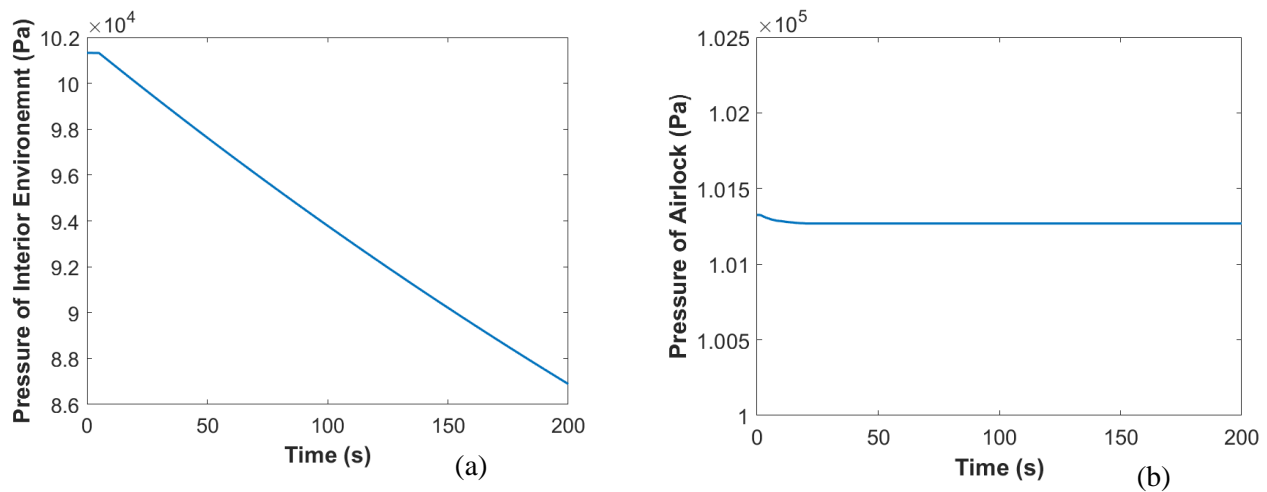


Figure 51. Pressure of HIEM (a) and the airlock (b) for meteorite intensity level 4

This hole causes the air mass of the interior environment to leave the system and enter the lunar atmosphere. The pressure and temperature therefore decrease as expected.

A meteorite impact with an intensity level of 5 has a hole radius of 0.008m through the interior environment. Figures 52 and 53 show the temperature and pressure of the interior environment and airlock.

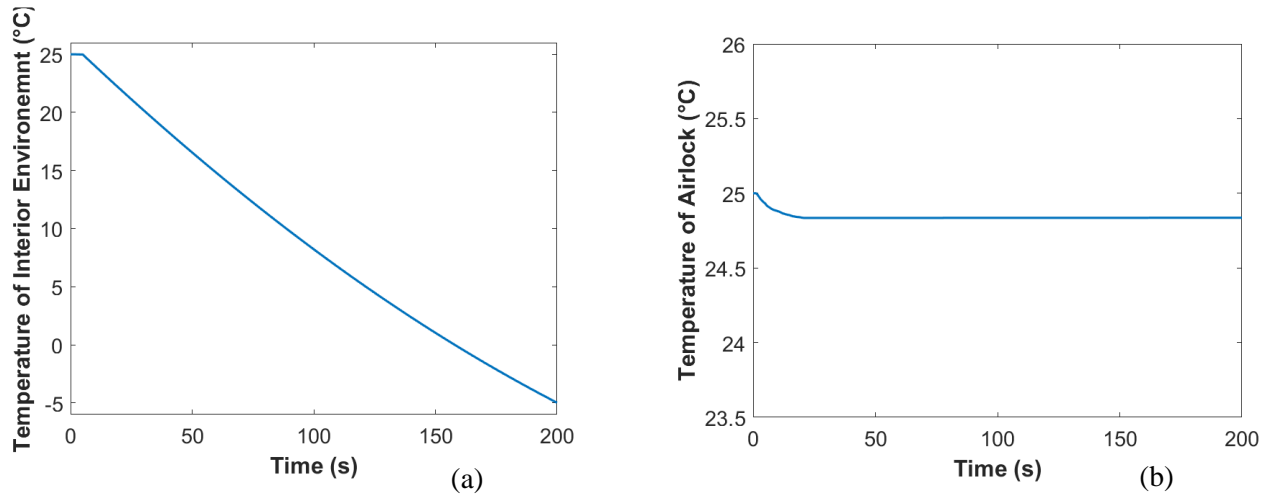


Figure 52. Temperature of HIEM (a) and the airlock (b) for meteorite intensity level 5

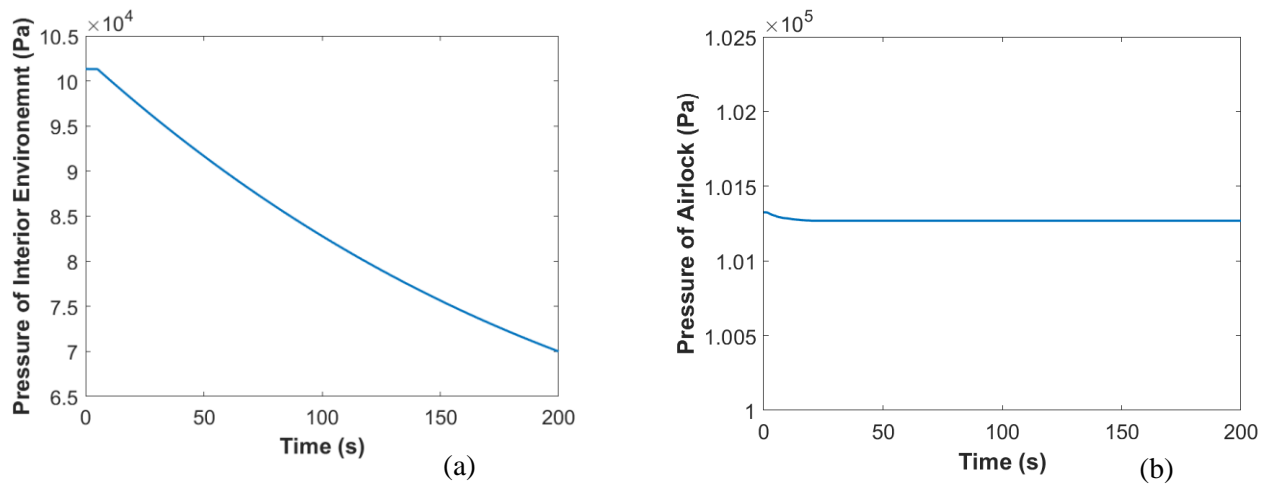


Figure 53. Pressure of HIEM (a) and the airlock (b) for meteorite intensity level 5

Comparing the results of meteorite intensities 4 and 5, it is evident that the increase in hole size has a corresponding increase in pressure and temperature decline.

An airlock failure with an intensity level of 2 has a hole radius of 0.002m on the airlock outer door. In this case, the airlock is initially at normal conditions until the leakage occurs. Once the leakage occurs, the inner door closes to preserve the interior environment. Figures 54 and 55 show the temperature and pressure of each zone.

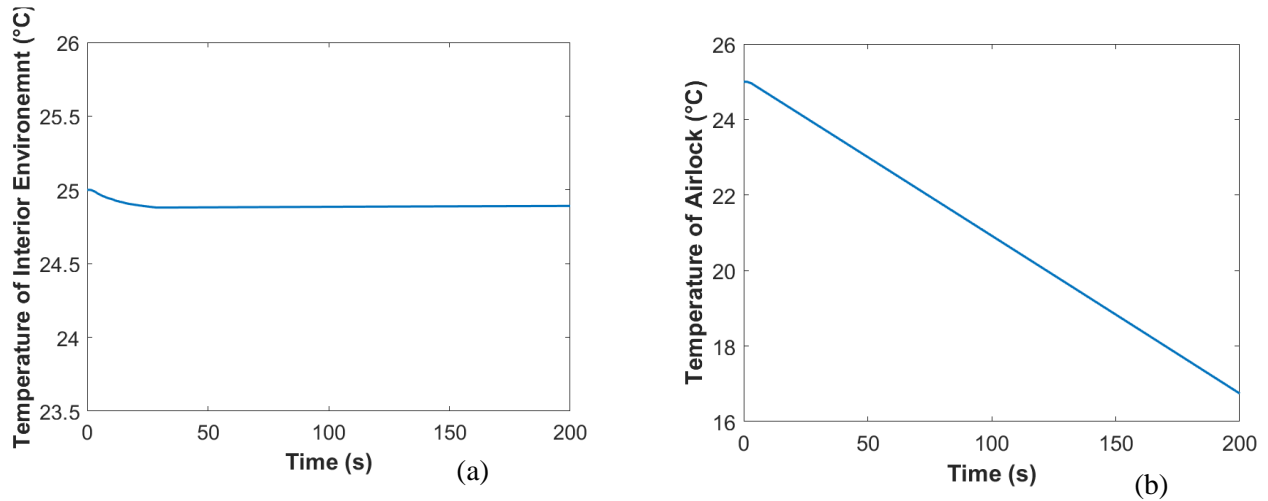


Figure 54. Temperature of HIEM (a) and the airlock (b) for airlock failure intensity level 2

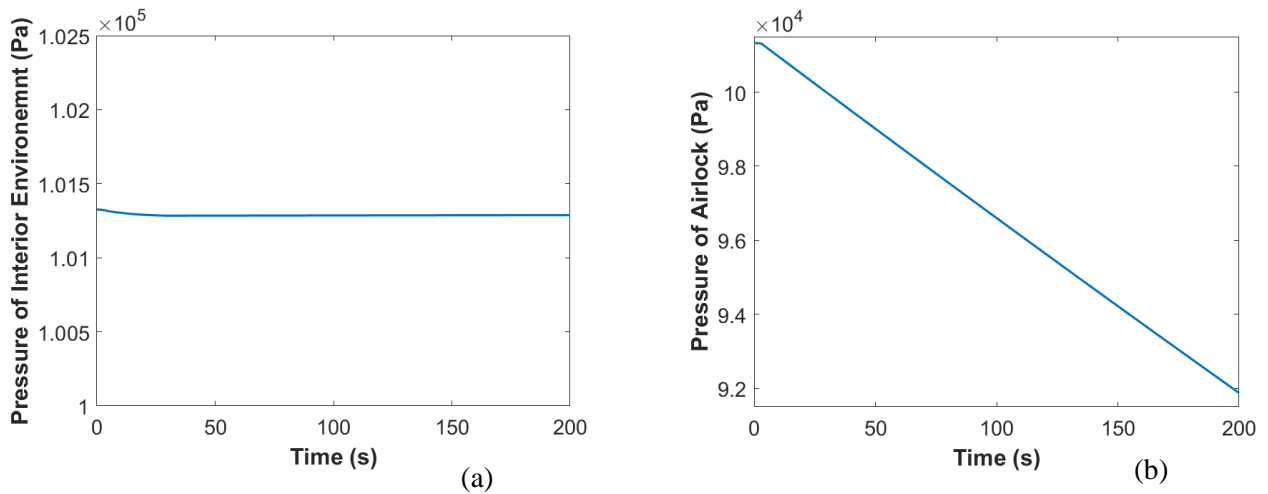


Figure 55. Pressure of HIEM (a) and the airlock (b) for airlock failure intensity level 2

In this scenario, the pressure leakage and temperature drop occur in the airlock chamber rather than the interior environment.

An airlock failure with an intensity level of 3 has a hole radius of 0.002 meters on the inner door. The scenario also occurs when the airlock is at a very low pressure—simulating when the airlock is in use for when an individual attempts to enter or exit from the outside. Since ECLSS has yet to create a system for the airlock, a mock ECLSS system was created in the HIEM to bring the airlock chamber to low pressures for this simulation. Figure 55 shows ECLSS providing a thermal load to the interior environment in an attempt to recover a comfortable range. Figures 57 and 58 show the

temperature and pressure of the interior environment and airlock for an airlock failure intensity 3.

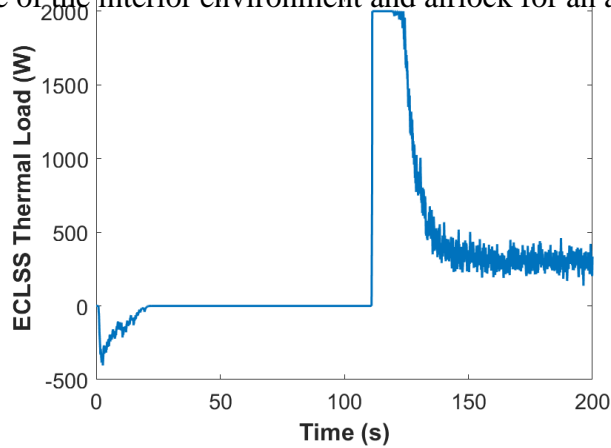


Figure 56. ECLSS thermal load for airlock failure intensity level 3

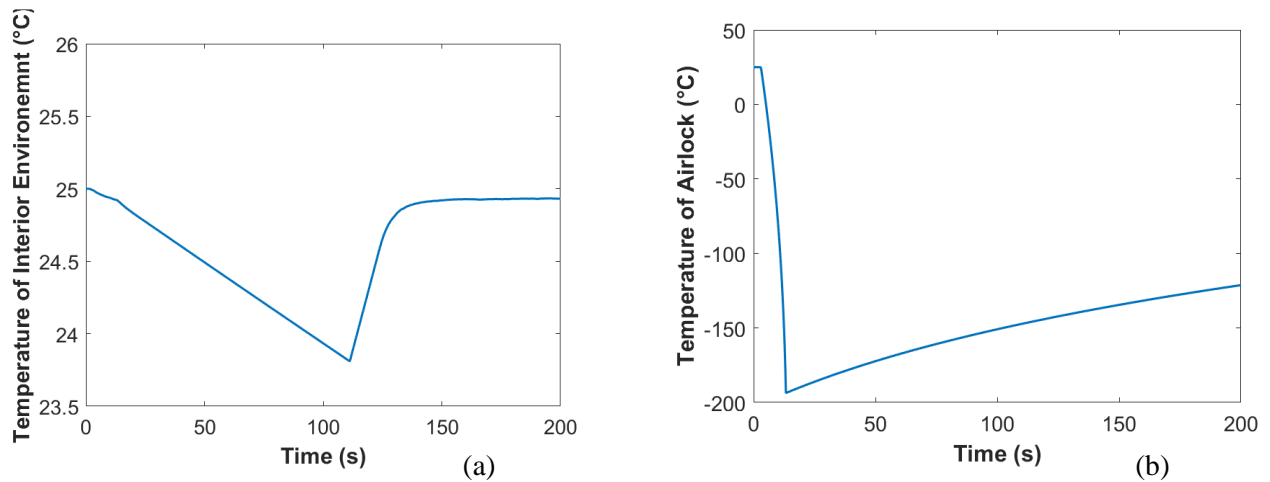


Figure 57-Temperature of HIEM (a) and the airlock (b) for airlock

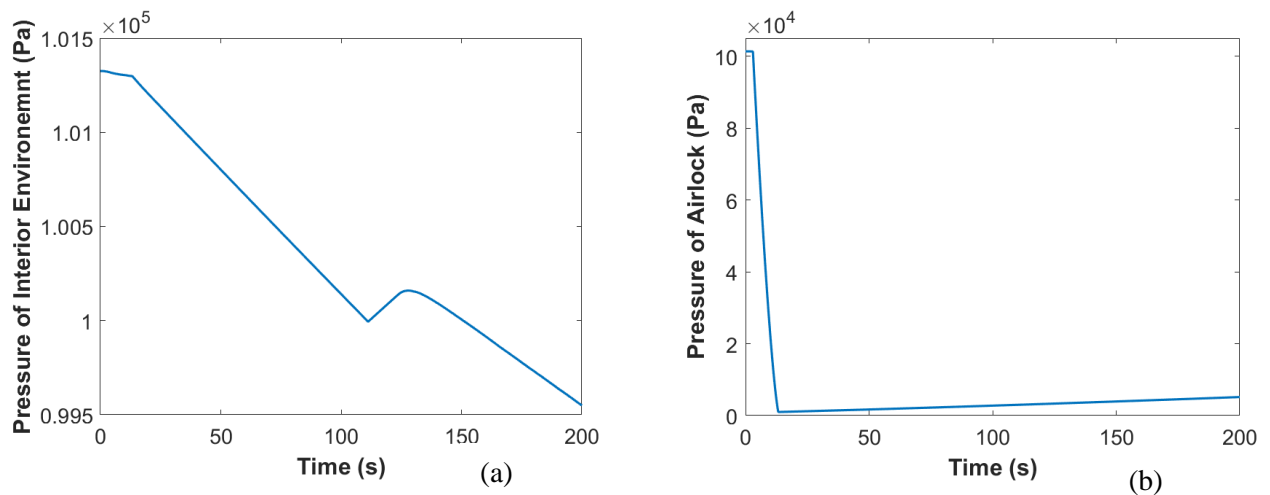


Figure 58-Pressure of HIEM (a) and the airlock (b) for airlock

failure intensity level 3

The steep drop in pressure for the airlock is the mock ECLSS bringing the airlock to near lunar

atmospheric pressures. Once the airlock is at a low pressure, the leakage occurs in the inner door. The increase in pressure and temperature can then be seen in the airlock graphs starting at 20 seconds. The slight increase in temperature and pressure in the interior environment after 100 seconds is due to ECLSS providing a thermal load to recover the temperature within a specific range. ECLSS never added air supply to the scenario because the interior environment is still within the pressure range allotted.

## **6. CONCLUSION AND FUTURE WORK**

The methodology used for HIEM uses a variety of equations largely based on conservation of energy and conservation of mass. The inputs of HIEM from ECLSS, structures, and the disturbance block affect the calculations used for temperature and pressure. HIEM then outputs these results to ECLSS and structures for further analysis within their models. The methodology used for HIEM was also applied to create a model of the pressure box used in CPT. The pressure leakage calculations employed in HIEM were quantitatively validated using experimental data from the pressure box. The pressure box model results are within an uncertainty range. The model with respect to temperature reveals that the behavior is slightly inconsistent with experimental results. This can most likely be contributed to the values used for resistances and capacitances. Further testing to obtain these values is needed to possibly improve model behavior accuracy. The use of a variable area flow meter in the pressure leakage studies proved challenging. It is not possible to determine the geometric area of leakage using this method. It is highly suggested to use a fixed area flow meter. By using a fixed area flow meter, there would then only be 2 unknowns ( $c_d$  and  $C_L$ ) and 2 equations (Equations 24 and 26) rather than 3 unknowns ( $c_d$ ,  $C_L$ , and  $A$ ) and 2 equations. Furthermore, CPT is adding another testing environment dubbed “the bladder”. The bladder is a dome-like structure larger than the pressure box. This bladder would be used for further cyber-physical testing. Pressure leakage scenarios similar to those aforementioned on the pressure box should also be conducted on the bladder.

Ultimately, validation of a fire scenario proves challenging for obvious reasons. There are many safety concerns involved in physical testing. Likewise, the bladder is a polyester material that melts at high temperatures. There have been discussions of adding heaters within the bladder to observe the behavior of the interior environment. Further discussions and considerations are needed to be able to validate the fire scenarios.

As for MCVT, various disturbance scenarios were tested using different intensity levels to qualitatively verify HIEM. As the fire intensity levels increase, so do the fire radii. This is reflected in the results of the temperature and pressure HIEM results. Similarly, as the meteorite intensity levels increase, so do the impact radius sizes. This leads to a larger pressure drop within the interior environment as seen in the results. With regards to the airlock failure scenarios, the results are consistent with predictions. For airlock failure intensity level 2, the temperature and pressure in

the airlock chamber decreases. Airlock failure intensity level 3 shows a decrease in temperature and pressure of the interior environment, but an increase in the airlock chamber.

There is a requirement to further expand HIEM. The interior environment in MCVT version 6.2 does not consider thermodynamic psychometrics. A humidity model will need to be employed in HIEM to accurately calculate the temperature of the interior environment. The model should also account for variations of gases such as CO<sub>2</sub>, O<sub>2</sub>, and N<sub>2</sub>. Furthermore, a two-zone model with an airlock, rather than a single zone and airlock model, is highly encouraged. The ability to separate the interior environment into two zones using a barrier would aid in the resiliency of the habitat. When a disturbance occurs in the interior environment, the barrier would then divide the habitat into two zones. One zone would be the safe zone while the other would be the damaged zone. The safe zone would be an area inhabitants could occupy while the agents repair the damaged zone. Once the damage is repaired, the barrier could go down. Furthermore, discussion among leadership and modelers will need to occur to decide if the structural subsystem will also provide the airlock interior wall temperature for the interior environment subsystem.

Overall, HIEM is a novel approach to predicting changes in the interior environment of structures due to different disruptions. With further improvements, the model would be able to predict the behavior of a lunar habitat's interior environment more accurately. It will also aid researchers in RETHi to determine ways to develop resiliency tactics for extraterrestrial applications.

## **APPENDIX A: TEST PROCEDURES**

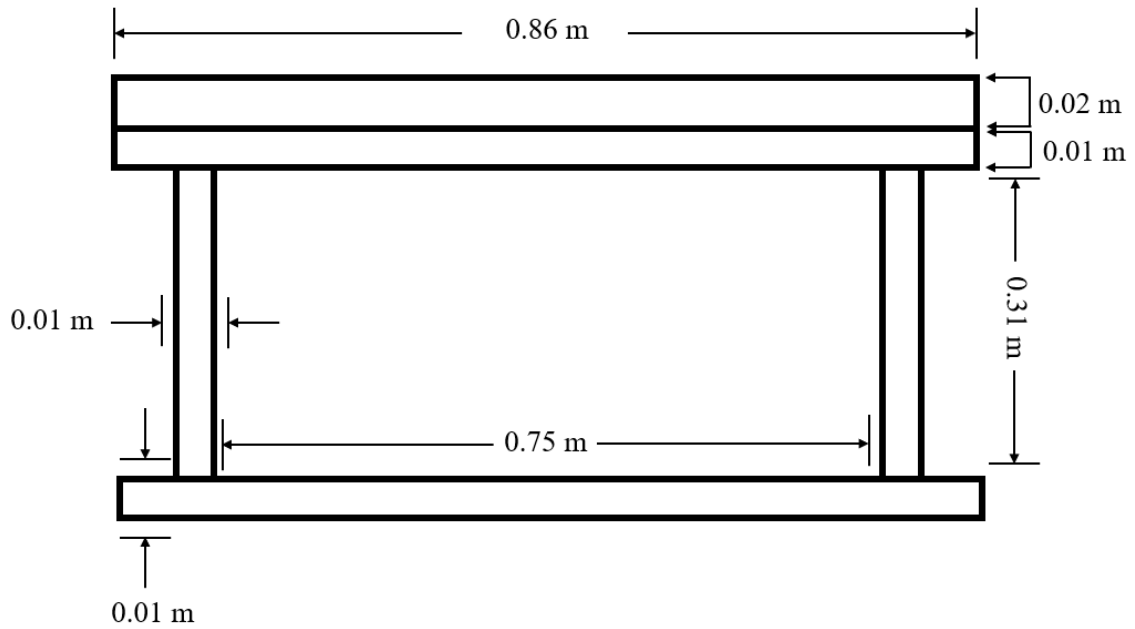
---

A1	Wear personal protection equipment. (glasses and ear protection)
A2	Turn on development computer (Dell Precision 3640)
A3	Open safety keybox and get the keys needed for your experiment - Insert the m+p dongle to the USB drive
A4	Open black cabinet and turn on DAQ modules (m+p hardware and speedgoat)
A5	Choose MATLAB (2020a) option in the speedgoat screen (real-time target machine)
A6	Open the m+p Hardware Selector application from the Desktop and choose the appropriate option a) NI for thermal experiments with the Mydax Chiller b) m+p VibRunner LAN devices for pressure experiments
A7	Load MATLAB R2020a, and type "slrt" in the Command Window. Make sure the status of the target machine shows "Connected = Yes"
A8	a) Open folder "C:\Thermal Transfer System\Transfer_system_2022\Speedgoat" for thermal experiments b) Open folder "C:\Thermal Transfer System\Pressure Regulator_Valve Testing" for pressure experiments
A9	a) Open Simulink model "Thermal_Transfer_System_v1_2.slx" for thermal experiments b) Open Simulink model "Wiring_Test_main.slx" for pressure experiments
<b>A1 Data Acquisition Setup - Thermal</b>	
A1-1	Left click on the file "Thermal_Transfer_setup1_2.sop5", and choose Open Outside MATLAB
A1-2	Left click on the file "mpAnalyzerApiOnlineData.csproj - Shortcut.lnk", and choose Open Outside MATLAB, and click start to run the project code. A pop-up window called m+p Analyzer API - Online Data will open.
A1-3	In the m+p Analyzer API - Online Data window click on Connect and make sure Connection Status shows: "Connected to m+p Analyzer". Click on Start Acquisition and make sure Status shows: "Running".
A1-4	Select "Function Type - Time record", "Response - All", "Reference - All" and check the "Continuous" box. Click Send Request.
A2-1	In the "Wiring_Test_main.slx" file, double click on the "Step Leakage Input" and give the final value from 0-10.
A2-2	Click on the "Run on Target" from Real-time top-ribbon and wait for the target monitor to initiate.
B1	Check for leaks around the chiller
B2	Turn Red handle in the front to turn on the chiller (with safety distance)
B3	Check that in the touch screen no error is showing
B4	Touch the white area of the screen, it will show the crankcase temperature. Wait for it to reach or surpass the Goal Temp.

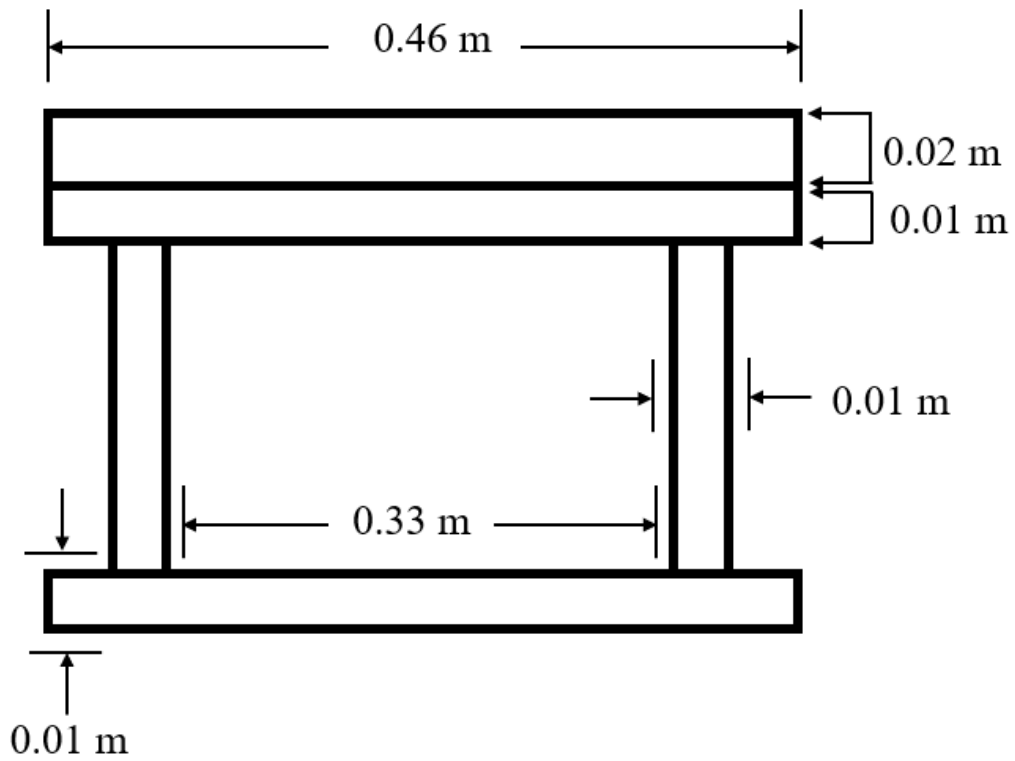
B6	Make sure the Condenser IN and OUT pipes at the back of the chiller are connected and check for leaks
B7	Make sure the Pump IN and OUT lines at the back of the chiller are connected and check for leaks
B8	Check the nitrogen regulator of the cylinder to supply nitrogen at 50 PSI
B9	Check the nitrogen regulator pressure on the tank to be between 8-10 PSI
B11	Check the oil level at the back of the chiller. Make sure it is slightly above or close to Full
B12	Open the water loop valves and check for leaks
B13	In the touch screen, select Loop 1 and adjust Flow Rate or Set Temperature accordingly
B1-1	Open the main supply (located in the vertical pipes by the pressure box) valves and check for leaks
B1-2	Adjust the bypass valve if needed (Usually already opened)
B1-3	Secure the area around the set up and connect the power supply of the bypass valve to the nearest power outlet
B1-4	Check whether there is any loose wires or disconnected thermocouples
B2-1	Open the main compressed air supply valve slowly and make sure no air comes out from the quick disconnect fitting of the hose
B2-2	Set up the pressure in the manual pressure regulator, by turning the knob in clockwise direction. Choose the appropriate working pressure for your experiment (usually 15 PSI)
B2-3	Connect the "quick disconnect" hose fitting to the pressure box inlet
B3-1	Close the pressure box main valve
B3-2	Set the pressure regulator to the minimum value by turning the knob in CCW direction
B3-3	Close the main compressed air supply valve
B5.1	Make sure the chiller is properly warmed up by resetting history in the touch panel (Crankcase temp > Goal Temp)
B5.2	Push the green start button to start the chiller
B5.3	Check the screen for any errors, alarms or warnings. If any appear, turn the chiller off and correct accordingly.
B5.4	Turn the sign "Test in Progress"

<b>C. Shutdown</b>	
	Stop all the data acquisition processes and collect all your data
C1.1	Stop the chiller (press the red stop button)
C1.2	Wait for 30 seconds for the pump to stop moving.
C1.3	Turn off the chiller by turning the red handle to horizontal position
C1.5	Close the condenser loop valves
C1.6	Turn the sign to "No Test in Progress"
C1.7	Check for leaks
C2.1	Close the main loop oil valves
C2.2	Turn off the power supply and disconnect any power surges and extensions from the outlets making sure no cable is blocking the way
D1	Push emergency stop button on the chiller
D2	Contact shop and call 911
D3	Fire extinguisher is next to the entrance to HERL90
D4	In case of heat transfer fluid leakage, find absorption material from the cabinet in HERL80

## **APPENDIX B: PRESSURE BOX DRAWING WITH DIMENSIONS**



**Front view**



**Side view**

## APPENDIX C: PRESSURE BOX RC VALUES

$R_{convection}$	1.61 hr-°F/Btu
$R_{radiation}$	3.15 hr-°F/Btu
$R_m$	1.25 hr-°F/Btu
$R_{steel}$	0.02 hr-°F/Btu
$R_{insulation}$	10.8 hr-°F/Btu
$C_{steel}$	6.79 Btu / °F
$C_m$	23.5 Btu / °F

## REFERENCES

- [1] Van Helden, Albert. “The Galileo Project: Science: Satellites of Jupiter.” *The Galileo Project / Science | Satellites of Jupiter*, [http://galileo.rice.edu/sci/observations/jupiter\\_satellites.html](http://galileo.rice.edu/sci/observations/jupiter_satellites.html).
- [2] Gingerich, Owen. “Galileo, the Impact of the Telescope, and the Birth of Modern Astronomy.” *Proceedings of the American Philosophical Society*, vol. 155, no. 2, 2011, pp. 134–41. *JSTOR*, <http://www.jstor.org/stable/23056830>. Accessed 27 Oct. 2022.
- [3] Williams, Matt. “What Is the Heliocentric Model of the Universe?” *Phys.org*, Phys.org, 5 Jan. 2016, <https://phys.org/news/2016-01-heliocentric-universe.html>.
- [4] *How Did the Planets Get Their Names? | Cool Cosmos*. <https://coolcosmos.ipac.caltech.edu/ask/196-How-did-the-planets-get-their-names->.
- [5] Howell, Elizabeth, and Vicky Stein. “Mars Missions: A Brief History.” *Space.com*, Space, 1 Mar. 2022, <https://www.space.com/13558-historic-mars-missions.html>.
- [6] History.com Editors. “The Space Race.” *History.com*, A&E Television Networks, 22 Feb. 2010, <https://www.history.com/topics/cold-war/space-race>.
- [7] “Comic Books #60: Mars and Beyond.” *Retrospace*, <https://www.retrospace.org/2013/09/comic-books-60-mars-and-beyond.html>.
- [8] Garcia, Mark. “NASA Station Astronaut Record Holders.” *NASA*, NASA, 3 May 2016, <https://www.nasa.gov/feature/nasa-station-astronaut-record-holders>.
- [9] Dyke, Shirley J, et al. RETHI, *Strategies for the Design and Operation of Resilient Extraterrestrial Habitats*, [https://www.purdue.edu/rethi/files/SPIE2021\\_submitted.pdf](https://www.purdue.edu/rethi/files/SPIE2021_submitted.pdf).
- [10] Van Buren, Brooks. “RETH Institute.” *RETHi at Purdue*, <https://www.purdue.edu/rethi/>.
- [11] MODULAR COUPLED VIRTUAL TESTBED (VERSION 6), RETHi NASA Annual Review, 27 May 2022
- [12] Maghareh, Amin & Lenjani, Ali & Krishnan, Murali & Dyke, Shirley & Bilonis, Ilias. (2021). Role of Cyber-Physical Testing in Developing Resilient Extraterrestrial Habitats. 1059-1068. 10.1061/9780784483374.098.
- [13] Gail D. Chittleborough, David F. Treagust, Why Models are Advantageous to Learning Science, *Educación Química*, Volume 20, Issue 1, 2009, Pages 12-17, ISSN 0187-893X, [https://doi.org/10.1016/S0187-893X\(18\)30003-X](https://doi.org/10.1016/S0187-893X(18)30003-X).

- [14] Zequn Wang, Yuxiang Chen, Yong Li, Development of RC model for thermal dynamic analysis of buildings through model structure simplification, *Energy and Buildings*, Volume 195, 2019, Pages 51-67, ISSN 0378-7788, <https://doi.org/10.1016/j.enbuild.2019.04.042>.
- [15] R.C. Johnson, M. Royapoor, M. Mayfield, A multi-zone, fast solving, rapidly reconfigurable building and electrified heating system model for generation of control dependent heat pump power demand profiles, *Applied Energy*, Volume 304, 2021, 117663, ISSN 0306-2619, <https://doi.org/10.1016/j.apenergy.2021.117663>.
- [16] Scialdone, John J. “Internal Pressures of a Spacecraft or Other System of Compartments, Connected in Various Ways and Including Outgassing Materials, in a Time-Varying Pressure Environment.” *NASA*, NASA, Aug. 1969, <https://ntrs.nasa.gov/>.
- [17] Aaron L. Jaffe, Gregory A. Kopp, Internal pressure modelling for low-rise buildings in tornadoes, *Journal of Wind Engineering and Industrial Aerodynamics*, Volume 209, 2021, 104454, ISSN 0167-6105, <https://doi.org/10.1016/j.jweia.2020.104454>.
- [18] Oh, J. H., Kopp, G. A., and Inculet, D. R. (2007). The UWO contribution to the NIST aerodynamic database for wind loads on low buildings: Part 3. Internal pressures. *J. WindEng. Ind. Aerodyn.* 95, 755–779. doi: 10.1016/j.jweia.2007.01.007
- [19] Holmes, J.D. (2015). *Wind Loading of Structures* (3rd ed.). CRC Press. <https://doi.org/10.1201/b18029>
- [20] Holmes, John D.. “MEAN AND FLUCTUATING INTERNAL PRESSURES INDUCED BY WIND.” (1980).
- [21] K. T. Walsh, J. Fielding, M. D. Smooke, and M. B. Long, “Experimental and computational study of temperature, species, and soot in buoyant and non-buoyant coflow laminar diffusion flames,” *Proceedings of the Combustion Institute*, vol. 28, no. 2, pp. 1973–1979, 2000.
- [22] Darling, David. “Quest Joint Airlock.” *The Worlds of David Darling*, [https://www.daviddarling.info/encyclopedia/Q/Quest\\_Joint\\_Airlock.html](https://www.daviddarling.info/encyclopedia/Q/Quest_Joint_Airlock.html).
- [23] “Latent and Sensible Heat.” *Latent and Sensible Heat | North Carolina Climate Office*, <https://legacy.climate.ncsu.edu/edu/Heat#:~:text=Latent%20and%20sensible%20heat%20are,with%20no%20change%20in%20phase>.
- [24] J. W. Mitchell and J. E. Braun, *Principles of heating, ventilation, and air conditioning in buildings*. Wiley, 2012.
- [25] Byström, Alexandra. “Compartment Fire Temperature: Calculations and Measurements.” *Luleå University of Technology*, Luleå University of Technology, Graphic Production, 2017.

- [26] Jaffer, Aubrey. “Convection from a Rectangular Plate.” *MIT CSAIL*, Massachusetts Institute of Technology, <https://people.csail.mit.edu/jaffer/SimRoof/Convection/>.
- [27] L. Zhao and K. Rezkallah, “Gas-liquid flow patterns at microgravity conditions,” *International Journal of Multiphase Flow*, vol. 19, no. 5, pp. 751–763, 1993, ISSN: 0301-9322. DOI: [https://doi.org/10.1016/0301-9322\(93\)90041-R](https://doi.org/10.1016/0301-9322(93)90041-R). [Online]. Available: <https://www.sciencedirect.com/science/article/pii/030193229390041R>.
- [28] T. Bourgeois, F. Ammouri, M. Weber, and C. Knapik, “Evaluating the temperature inside a tank during a filling with highly-pressurized gas,” *international journal of hydrogen energy*, vol. 40, no. 35, pp. 11 748–11 755, 2015.
- [29] M. J. Moran, *Fundamentals of Engineering Thermodynamics*, 9th Edition. John Wiley amp; Sons, 2018.
- [30] S. Bendapudi, J. E. Braun, and E. A. Groll, “A comparison of moving-boundary and finite-volume formulations for transients in centrifugal chillers,” *International journal of refrigeration*, vol. 31, no. 8, pp. 1437–1452, 2008.
- [31] I. H. Bell, J. Wronski, S. Quoilin, and V. Lemort, “Pure and pseudo-pure fluid thermophysical property evaluation and the open-source thermophysical property library coolprop,” *Industrial & engineering chemistry research*, vol. 53, no. 6, pp. 2498–2508, 2014.
- [32] I. H. Bell, E. W. Lemmon, and A. H. Harvey, “Algorithms for the calculation of psychrometric properties from multi-fluid helmholtz-energy-explicit models,” *International Journal of Refrigeration*, vol. 87, pp. 26–38, 2018, ISSN: 0140-7007. DOI: <https://doi.org/10.1016/j.ijrefrig.2017.10.001>. [Online]. Available: <https://www.sciencedirect.com/science/article/pii/S014070071730381X>.
- [33] Park, Jaewon. “Development of a Cyber-Physical Testbed for Resilient Extra-Terrestrial Habitats.” *Purdue University School of Mechanical Engineering West Lafayette, Indiana May 2022*, 2022.
- [34] Winters, William S., Evans, Gregory H., Rice, Steven F., and Greif, R. *An Experimental and Theoretical Study of Heat and Mass Transfer during the Venting of Pressure Vessels*. United States: N. p., 2010. Web.
- [35] Brahma I (2019) Measurement and Prediction of Discharge Coefficients in Highly Compressible Pulsating Flows to Improve EGR Flow Estimation and Modeling of Engine Flows. *Front. Mech. Eng.* 5:25. doi: 10.3389/fmech.2019.00025